iScience

CellPress
OPEN ACCESS

Article

Dendritic peptide-conjugated polymeric nanovectors for non-toxic delivery of plasmid DNA and enhanced non-viral transfection of immune cells

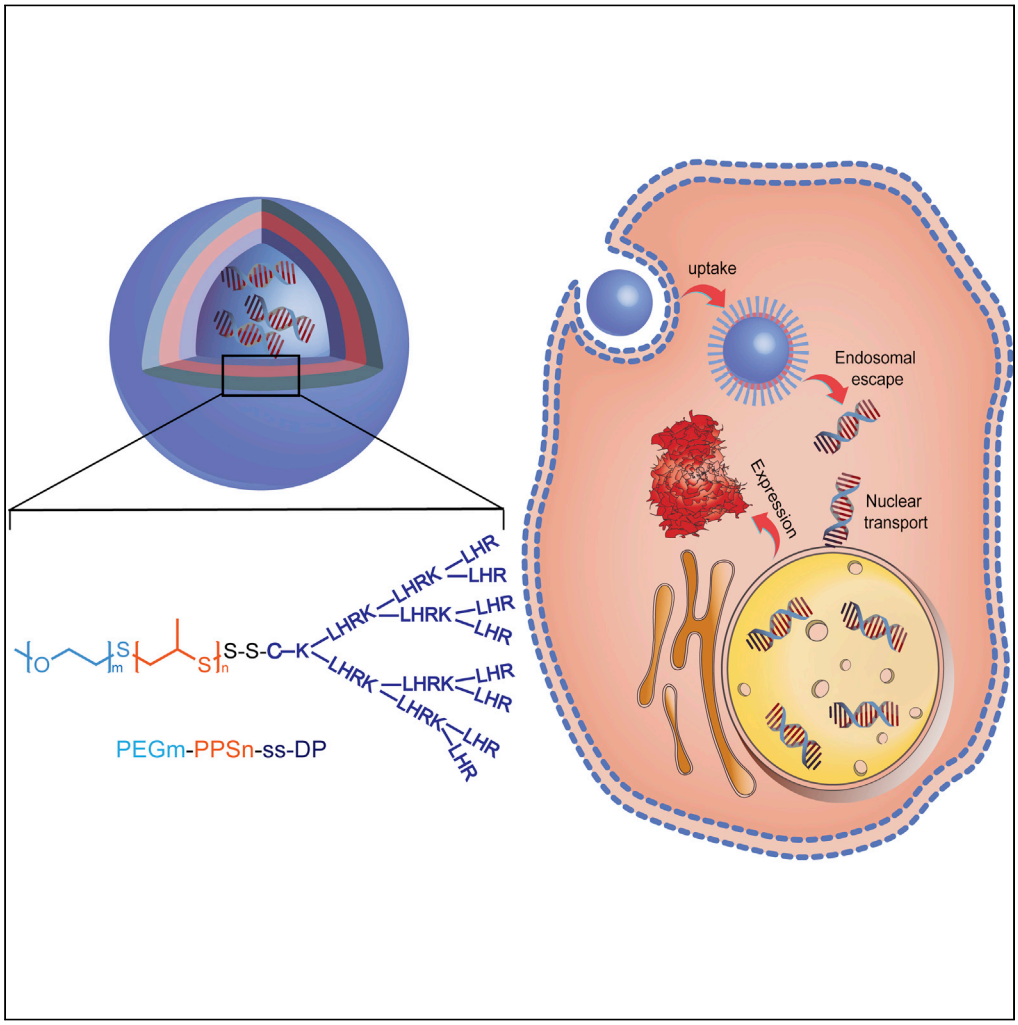

Sijia Yi, Sun-Young Kim, Michael P. Vincent, Simseok A. Yuk, Sharan Bobbala, Fanfan Du, Evan Alexander Scott

evan.scott@northwestern.edu

Highlights

A polymeric delivery system for plasmid transfection of immune cells is optimized

CRISPR/Cas9 plasmid transfection is achieved without toxicity or specialized media

Immune cells are transfected more efficiently compared to a leading transfection reagent

Yi et al., iScience 25, 104555
July 15, 2022
https://doi.org/10.1016/j.isci.2022.104555

iScience

CellPress
OPEN ACCESS

Article

Dendritic peptide-conjugated polymeric nanovectors for non-toxic delivery of plasmid DNA and enhanced non-viral transfection of immune cells

Sijia Yi,[1,7] Sun-Young Kim,[1,2,7] Michael P. Vincent,[1] Simseok A. Yuk,[1] Sharan Bobbala,[3] Fanfan Du,[1] and Evan Alexander Scott[1,4,5,6,8,*]

SUMMARY

Plasmid DNA (pDNA) transfection is advantageous for gene therapies requiring larger genetic elements, including "all-in-one" CRISPR/Cas9 plasmids, but is limited by toxicity as well as poor intracellular release and transfection efficiency in immune cell populations. Here, we developed a synthetic non-viral gene delivery platform composed of poly(ethylene glycol)-*b*-poly(propylene sulfide) copolymers linked to a cationic dendritic peptide (DP) via a reduceable bond, PEG-*b*-PPS-ss-DP (PPDP). A library of self-assembling PPDP polymers was synthesized and screened to identify optimal constructs capable of transfecting macrophages with small (pCMV-DsRed, 4.6 kb) and large (pL-CRISPR.EFS.tRFP, 11.7 kb) plasmids. The optimized PPDP construct transfected macrophages, fibroblasts, dendritic cells, and T cells more efficiently and with less toxicity than a commercial Lipo2K reagent, regardless of pDNA size and under standard culture conditions in the presence of serum. The PPDP technology described herein is a stimuli-responsive polymeric nanovector that can be leveraged to meet diverse challenges in gene delivery.

INTRODUCTION

Recent progress in genetic engineering has resulted in materials and methods for improved cancer immunotherapy (Riley et al., 2019; Vincent et al., 2022), antiviral therapies (Larocca et al., 2016), and DNA vaccines (Smith et al., 2020), as well as non-medical applications (Chang et al., 2018). Notwithstanding a large number of ongoing trials in the area of genome editing, successful gene therapy products remain limited (Cornu et al., 2017; Dunbar et al., 2018; Li et al., 2020). This is largely due to various challenges surrounding the effective transport and expression of nucleic acids within target cells. An efficient nucleic acid delivery system must provide protection from enzymatic degradation while achieving efficient cellular internalization, escape from endo-lysosomes, and cytosolic cargo release. Plasmid-based gene therapy is a promising transfection strategy that is capable of delivering CRISPR/Cas9 (Cong and Zhang, 2015; Knott and Doudna, 2018; Liu et al., 2017) for stable genome editing using an all-in-one plasmid approach (Yip, 2020). However, naked plasmid DNA (pDNA) has many obstacles (Shi et al., 2017; Song et al., 2017) for cellular uptake owing to its negative charge, large molecular size that limits delivery via viral vectors, and low encapsulation efficiency in synthetic nanocarriers.

As natural gene delivery vehicles, viruses efficiently modulate gene expression; however, various issues (David and Doherty, 2017), such as insertional mutagenesis (Baldo et al., 2013), inherent immunogenicity (Shirley et al., 2020), and pre-existing host antibodies against viral components (Nidetz et al., 2020), can reduce their efficacy and utility in clinical settings (Goswami et al., 2019). Importantly, the limited DNA-carrying capacity (<8 kb) (Nayerossadat et al., 2012) and manufacturing challenges (Ayuso, 2016; Moleirinho et al., 2020; Srivastava et al., 2021; van der Loo and Wright, 2016) pose additional restrictions for viral-based vectors. Non-viral vectors and synthetic carriers, including lipids, polymers, peptides, and inorganic nanomaterials have, therefore, attracted increasing attention owing to their tunable immunogenicity, flexible packaging capacity, amenability to scalable fabrication methods, and access to diverse mechanisms of intracellular delivery for improved transfection efficiency (Hil et al., 2016; Ramamoorth and Narvekar,

[1]Department of Biomedical Engineering, Northwestern University, Evanston, IL 60208, USA

[2]SKKU Advanced Institute of Nanotechnology (SAINT), Sungkyunkwan University (SKKU), 2066 Seobu-ro, Jangan-gu, Suwon-si, Gyeonggi-do 16419, Republic of Korea

[3]Department of Pharmaceutical Sciences, School of Pharmacy, West Virginia University, Morgantown, WV 26505, USA

[4]Simpson Querrey Institute, Northwestern University, Chicago, IL 60611, USA

[5]Robert H. Lurie Comprehensive Cancer Center, Northwestern University, Chicago, IL 60611, USA

[6]Department of Microbiology-Immunology, Northwestern University, Chicago, IL 60611, USA

[7]These authors contributed equally

[8]Lead contact

*Correspondence: evan.scott@northwestern.edu

https://doi.org/10.1016/j.isci.2022.104555

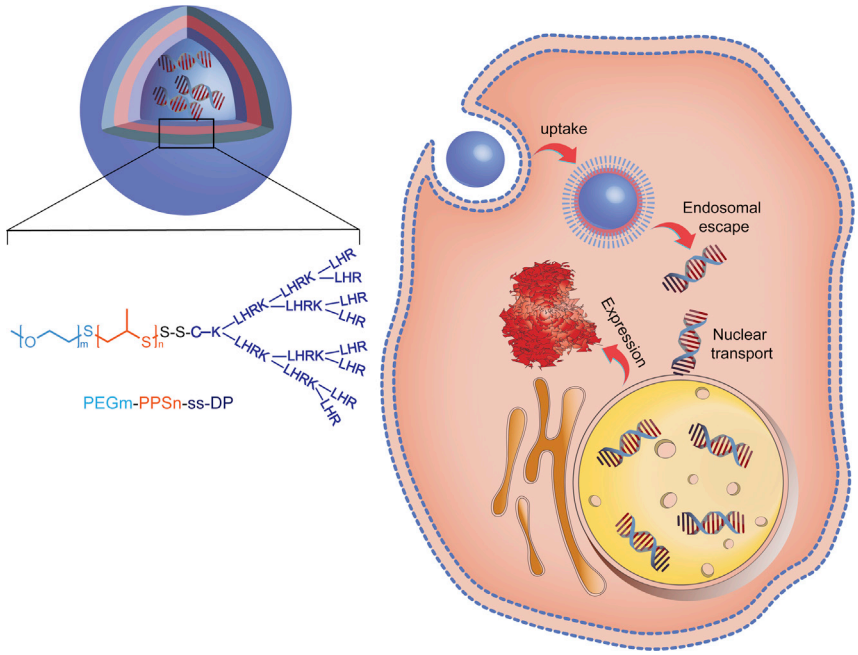

Figure 1. The design and structure of the PEG$_m$-*b*-PPS$_n$-ss-DP (PPDP) gene delivery system
The general strategy for enhancing the intracellular release of plasmid DNA (pDNA) is illustrated.

2015; Shi et al., 2017; Vincent et al., 2022; Zhang et al., 2012). However, existing materials still face challenges such as inefficient endosomal escape, substantial toxicity, and low gene transfection/cellular expression. The issue of low transfection is especially problematic for certain cell types, particularly immune cells that are high-value targets for diverse therapeutic applications including vaccination and cancer immunotherapy. Cationic lipids are the most widely used non-viral vectors for nucleic acid delivery in immortalized cell lines, yet many blood and immune cells remain recalcitrant (Stewart et al., 2016). Lipid-based technologies aside, many polymeric transfection reagents, such as polyethylenimine (PEI), have long suffered from cytotoxicity concerns (Boussif et al., 1995; Fischer et al., 1999; Godbey et al., 1999). Furthermore, numerous cell types that include primary cells and immune cells are highly sensitive to their culture conditions, yet the most common *in vitro* transfection agents, lipofectamine for example, require specialized serum-free medium. Thus, there is high demand for alternative technologies capable of delivering nucleic acids intracellularly to difficult-to-transfect cells under their standard culture conditions without associated increases in toxicity.

Dendritic or branched cationic peptides have a three-dimensional (3D) architecture with multiple functional groups, which makes them well suited for delivering negatively charged nucleic acids (Xu et al., 2014; Zeng et al., 2015). Dendritic structures can significantly enhance the interaction of peptides with DNA, considerably improve cargo packing, and increase the transfection efficiency in diverse cell types, compared to linear DNA-binding peptides (Zhou et al., 2016). A variety of parameters influence the activity and biocompatibility of dendritic peptides (DPs), including molecular weight, functionality of branching units, and charge distribution (Abbasi et al., 2014; Kwok et al., 2013; Malik et al., 2000; Wang and Chen, 2017; Zeng et al., 2015). Notably, third-generation peptide dendrimers with lower molecular weight-to-charge ratios and charge distributed over the whole dendritic structure can be leveraged as efficient transfection reagents for DNA delivery (Kwok et al., 2013). Despite their potential, cationic peptide dendrimers form complexes with nucleic acids primarily through electrostatic interactions, which are generally unstable in serum when used alone and have potential cytotoxicity concerns (Madaan et al., 2014), limiting their application in gene therapy.

Here, we develop a gene delivery system employing self-assembling block copolymer nanocarriers engineered for efficient cytosolic delivery of pDNA via incorporation of a cationic DP block (Figure 1). We have previously demonstrated that poly (ethylene glycol)-block-poly (propylene sulfide) (PEG-*b*-PPS)

nanocarriers effectively target macrophages and dendritic cells (Vincent et al., 2021a; Yi et al., 2016, 2019), are capable of delivering diverse payloads intracellularly (Allen et al., 2017, 2018a bib_Allen_et_al_2017; Bobbala et al., 2020; Scott et al., 2012; Stack et al., 2020, 2021; Vasdekis et al., 2012; Vincent et al., 2021c), are non-immunogenic in human blood (Vincent et al., 2021b), and are both non-inflammatory and non-toxic in non-human primates (Allen et al., 2018b), humanized mice (Dowling et al., 2017), and diverse mouse models of disease (Yi et al., 2016). Furthermore, PEG-*b*-PPS copolymers can be formulated to permit the rapid self-assembly of nanostructures encapsulating biologic payloads upon the addition of aqueous medium (Bobbala et al., 2021), which extends their practical usage to industrial or clinical settings. Our present work is motivated by natural viruses possessing capsid proteins that utilize positively charged regions to carry and protect genes internally, which encapsulate this genetic material within a higher order protein framework/structure that is largely stabilized by non-covalent interactions between hydrophobic regions (Perlmutter and Hagan, 2015; Requião et al., 2020; Rossmann, 2013). We hypothesized that the high stability of hydrophobic PPS membranes and volumetric differences between the PEG and DP blocks would allow similar sequestration of large genetic elements within the interior of self-assembled PEG-*b*-PPS nanocarriers.

PEG-*b*-PPS copolymer was modified with a functional, cationic DP using a cysteine linker (PEG_m-*b*-PPS_n-ss-DP, PPDP) (Figure 1). Each unit of the DP is composed of lysine for functional unit branching, lipophilic leucine to help bind membranes and facilitate escape from endolysosomal compartments (Summerton, 2005), a histidine residue for its buffering capacity and to assist the disruption of endosomal membranes (Summerton, 2005), and arginine to stably interact with negatively charged DNA. The arginine residues complex with anionic nucleic acids under diverse conditions, as they are positively charged in the extracellular environment (prior to internalization) and at all pH conditions encountered within the endolysosomal pathway following cellular internalization. In addition to the peptide aspects of our technology, the PEG-*b*-PPS polymers contribute multiple useful features for gene delivery. For example, PEG-*b*-PPS provides oxidation sensitivity via its hydrophobic PPS blocks that stabilize the nanostructure and enable disassembly within acidic endolysosomal compartments (Bobbala et al., 2020; Scott et al., 2012; Stack et al., 2020; Vasdekis et al., 2012; Vincent et al., 2021c). The hydrophilic methoxy-terminated PEG corona serves to improve biocompatibility and reduce toxicity (Allen et al., 2018b; Vincent et al., 2021b). Furthermore, we incorporated a biologically reducible disulfide bond between the terminus of PPS and the DP to improve the release of DP-bound pDNA from PEG-*b*-PPS nanocarriers within reductive intracellular compartments.

We synthesized a library of self-assembling PPDP polymers and thoroughly examine their functionality as non-viral nanovectors for gene delivery. Cellular transfection experiments were benchmarked against a leading commercial product, Lipofectamine 2000 (Lipo2K). Furthermore, to understand whether our gene delivery platform is compatible with a range of DNA cargo sizes, we examined the transfection efficiency of a small DNA plasmid (S-pDNA; pCMV-DsRed, 4.6 kb) and a large DNA plasmid (L-pDNA; pL-CRISPR.EFS.tRFP, 11.7 kb). After conducting a comprehensive screen of PPDP-mediated transfection performance in macrophages as a model immune cell type, we optimize the formulation of the top performing nanovectors and elucidate the mechanistic details of their functionality in a series of multidisciplinary studies. Finally, the efficacy of the optimal PPDP nanovectors is assessed in NIH 3T3 fibroblasts, as well as a variety of difficult-to-transfect immune cell types, including T cells and primary bone marrow-derived dendritic cells (BMDCs).

RESULTS AND DISCUSSION

Synthesis and characterization of PEG-*b*-PPS-ss-DP polymer variants

To investigate the hydrophobic effects of PPDP on nanostructure self-assembly and supporting functional gene transfection, we synthesized a family of six PEG_m-*b*-PPS_n diblock copolymers that differed in the length of their PEG (750 or 2000 g/mol) and PPS blocks (Figure S1). The length of PPS ranged from 20 to 80 units. The PEG_m-*b*-PPS_n polymers were end-capped with pyridyl disulfide (PEG_m-*b*-PPS_n-pds) and characterized by ^{1}H NMR (Figure S2A). Each PEG_m-*b*-PPS_n-pds variant was conjugated to the cysteine-containing DP via sulfide exchange. Conjugation was verified by gel permeation chromatography (GPC), which demonstrated an increased molecular weight of the polymer (Figures S2B and S2C). To simplify the nomenclature in this study, the PEG_m-*b*-PPS_n-ss-DP polymer variants that differed in their molecular weight and hydrophobicity are designated from PPDP2 to PPDP7.

The PPDP library was self-assembled into stable nanostructures by simple mixing in the aqueous solution. The size distribution and zeta potential of PPDP polymers were measured by dynamic light scattering (DLS)

and Electrophoretic light scattering (ELS), respectively (Table S1). The nanostructures formed from PPDP2-PPDP7 polymers differed in size (from ~20 to 30 nm) and zeta potential (from ~10 to 40 mV) depending on the distinct combination of PEG molecular weight and PPS length of the polymer variant. Furthermore, small-angle X-ray scattering (SAXS) performed using synchrotron radiation demonstrated the presence of a spherical core-shell morphology (Figure S3 and Table S2).

Benchmarking PEG-*b*-PPS-ss-DP transfection performance and cytotoxicity in macrophages

PEG-b-PPS-ss-DP2 and PEG-*b*-PPS-ss-DP 5 achieve significantly greater transfection efficiency and reporter protein expression levels than Lipo2K

We next performed a series of screens in cultured RAW 264.7 macrophages to evaluate the performance of each PPDP nanovector as a gene delivery vehicle. Transfection using industry-standard Lipo2K following manufacturer recommendations was used to benchmark the performance of the PPDP platform. Furthermore, to understand whether PPDP permits the transfection of pDNA of a diverse size range, screens were performed using plasmids of two different molecular weights. S-pDNA (pCMV-DsRed, 4.6 kb) was used as a model small plasmid (Figures 2A–2C and S4A), which uses a CMV (cytomegalovirus) promoter to drive the expression of the DsRed fluorescent protein. L-pDNA (pL-CRISPR.EFS.tRFP, 11.7 kb) was used as a model large plasmid (Figures 2D–2F and S4B), which contains an EFS (elongation factor 1α short) promoter and co-expresses RFP together with the Cas9 protein. PPDP/pDNA complexes were formed by gently pipetting pre-formed PPDP nanostructures with plasmids followed by 30 min of mixing at room temperature. The transfection efficiency was determined after a 48 h incubation period by calculating the percentage of transfected cells using flow cytometry. The expression level of the plasmid-encoded fluorescent protein was also quantified to understand the extent of transfection (Figures 2C, 2F, and S4).

The transfection efficiency of S-pDNA using PPDP2 and PPDP5 was significantly higher than any other PPDP nanostructure and commercial transfection agent (Lipo2K), with roughly 45% of DsRed-positive cells transfected with PPDP2/S-pDNA and 25% of DsRed-positive cells transfected with PPDP5/S-pDNA (Figures 2B and S4A). This PPDP screen further revealed that only PPDP2 and PPDP5 achieved significantly greater transfection efficiencies than Lipo2K (Figure 2B). Furthermore, S-pDNA transfection with PPDP2 was significantly more efficient than that achieved by PPDP5 and all other PPDP constructs examined (Figure 2B). Comparable trends were observed when examining the extent of DsRed protein expression (Figure S4A). In the transfection efficiency vs. protein expression level coordinate, the PPDP2 and PPDP5 achieved values in the upper quadrant, whereas Lipo2K and all other nanovectors clustered together in a lower performing region (Figure 2C).

Consistent with the S-pDNA results, both PPDP2 and PPDP5 were also more robust than Lipo2K in delivering a substantially larger plasmid, denoted here as L-pDNA (Figures 2D and S4B). Macrophages were transfected with the large L-pDNA plasmid at high efficiencies of 47 and 40% when delivered using PPDP2 and PPDP5, respectively (Figure 2E). Strikingly, the PPDP2 transfection efficiency was ~10 times greater than that of Lipo2K (4.8% of RFP positive cells) (Figure 2E). PPDP2 again performed significantly better than Lipo2K and all other PPDP constructs in these studies using the larger L-pDNA plasmid, achieving significantly greater RFP reporter expression levels (Figures 2F and S4B).

The PEG-b-PPS-ss-DP platform is less cytotoxic than commercial Lipo2K and polyethylenimine reagents

Cytotoxicity of PPDP and PPDP/pDNA nanocomplexes prepared at various weight ratios was examined in RAW 264.7 macrophage cells (Figures S5, 3A, and 3B). The cytotoxicity of PPDP/pDNA nanocomplexes was examined using the 3-(4,5-dimethylthiazol-2-yl)-2,5-diphenyltetrazolium bromide (MTT) assay. These toxicity studies were benchmarked against both Lipo2K, which is the leading commercially available transfection reagent, and the cationic PEI polymer. PEI (25 kDa) was included as a control, as it is a widely used polymeric transfection reagent that has known toxicity concerns (Boussif et al., 1995; Fischer et al., 1999; Godbey et al., 1999).

PPDP/pDNA nanocomplexes were generally non-toxic (cell viability >80%) under weight ratio of 60:1 (PPDP: both S-pDNA and L-pDNA), whereas cell viability was lower for nanocomplexes having a PPDP/pDNA ratio of 120:1 (Figure 3). However, decreases in cell viability were also observed for the unconjugated DP peptide, even at a peptide/S-pDNA weight ratio of less than 60:1. These results suggest that conjugating DP to PEG-*b*-PPS copolymer significantly reduces the toxicity of the peptide. Importantly, the cytotoxicity of PPDP/pDNA nanocomplexes was much lower than the commercial polymeric transfection agent

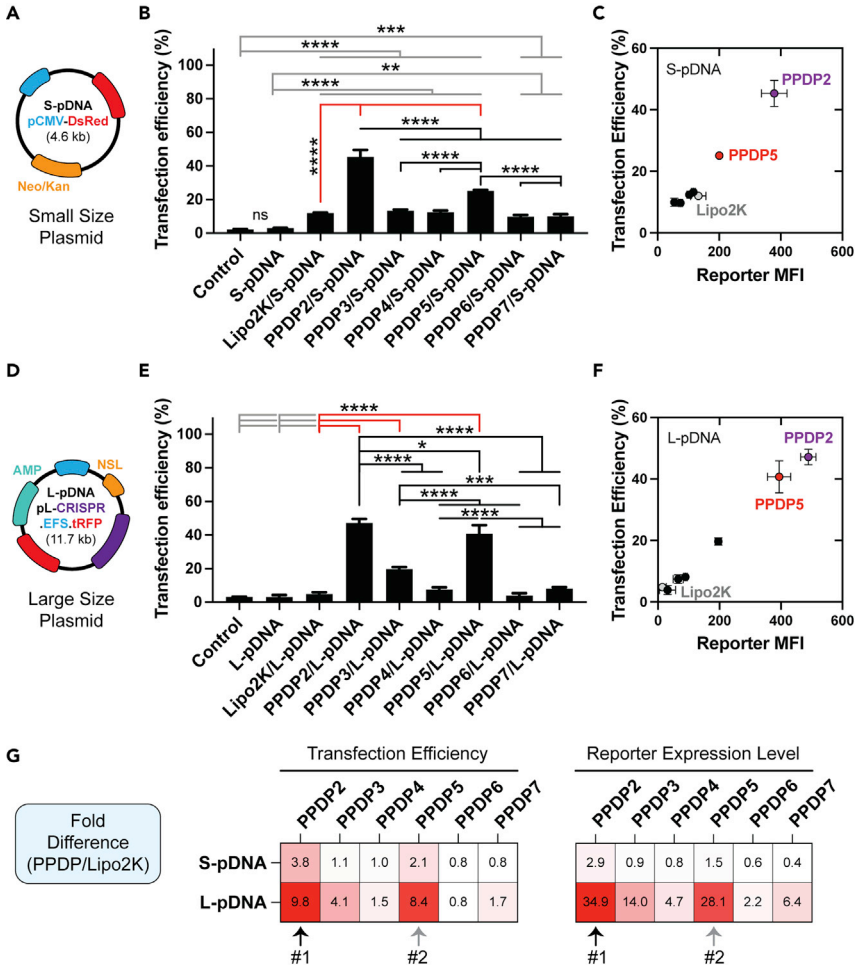

Figure 2. PPDP2 and PPDP5 achieve higher plasmid DNA transfection efficiencies and reporter expression levels than Lipo2K in a macrophage-based screen

RAW 264.7 macrophages were incubated with the specified materials for 48 h.

(A) Schematic of the model small size plasmid DNA (pCMV-DsRed, 4.6 kb), containing a CMV promoter and a DsRed reporter gene.

(B) Transfection efficiency of S-pDNA using PPDP nanovectors (PPDP2-PPDP7) quantified as the percentage of cells expressing fluorescent reporter proteins.

(C) Transfection efficiency of S-pDNA plotted with the mean fluorescence intensity (MFI) of cells expressing the DsRed reporter.

(D) Schematic of the model large size plasmid DNA (pL-CRISPR.EFS.tRFP, 11.7 kb) used in this study, containing an EFS promoter with NSL, Cas9, and RFP reporter genes.

(E) Transfection efficiency of L-pDNA by PPDP nanovectors.

(F) Transfection efficiency and MFI of cells expressing the RFP reporter.

(G) Fold difference in the PPDP-mediated plasmid transfection efficiency (left) and reporter expression level (right) compared to Lipo2K. The rank of PPDP2 and PPDP5 is annotated below each heatmap. In all cases, a 60:1 PPDP:pDNA weight ratio was used. Data are presented as the mean ± SD (n = 3). Transfections using were performed per manufacturer instructions. For panels (b, e), significant differences were determined by ANOVA with *post hoc* Tukey's multiple comparisons test (5% significance level). *$p < 0.05$, **$p < 0.005$, ***$p < 0.001$, ****$p < 0.0001$. Comparisons to control and pDNA (gray bars), Lipo2k (red bars), and within PPDP treatment groups (black bars) are presented in the specified colors.

PEI (Figure 3). High (~90–100%) cell viability was observed for PPDP2 up to the 60:1 polymer-to-pDNA ratio for both large and small plasmids, which was generally less cytotoxic than PPDP5 (Figures 3 and S5).

Collectively, the results from our screening studies demonstrate that PPDP2 and PPDP5 are technologies that outperform the industrial standard transfection reagents. Given the longer hydrophobic PPS lengths of

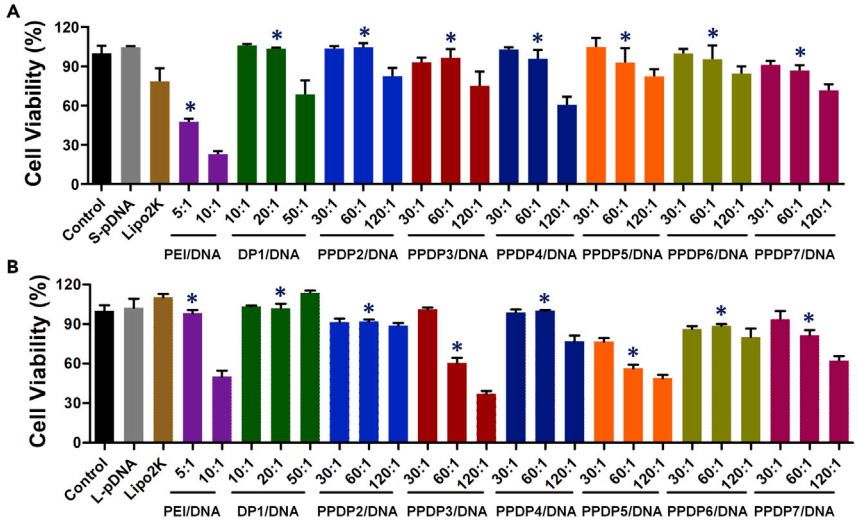

Figure 3. Cytotoxicity of PPDP/pDNA nanovector in RAW 264.7 macrophages

RAW 264.7 macrophages were incubated with PPDP/pDNA nanocomplexes that were prepared with a different polymer to pDNA ratios (30:1, 60:1, 120:1) for 24 h at 37 °C. Untreated cells (Control), Lipo2K/pDNA complexes (Lipo2K), PEI/pDNA complexes (PEI with the molecular weight of 25 kDa), and dendritic peptide (DP)/pDNA complexes were included as benchmarks. The cell viability for (a) PPDP/S-pDNA complexes and (b) PPDP/L-pDNA complexes was then measured by the MTT assay. Asterisks indicate the experimentally determined optimal ratio for each formulation. Data are presented as the mean ± SD (n = 3).

PPDP2 (80 units) and PPDP5 (74 units) compared to the other more toxic PPDP polymer variants, the increased hydrophobicity may play a role in reducing toxicity, possibly by modulating the structure and/or stability of the complexes. The emergence of PPDP2 and PPDP5 from these initial screening efforts led us to focus subsequent development efforts around these prototypes. The proceeding work emphasized the PPDP2 nanovector, as it outperformed all other prototypes by a large margin, including PPDP5 (Figures 2C, 2F, and 2G). Furthermore, PPDP2 performed at a higher level while exhibiting even lower cytotoxicity than PPDP5 (Figure 3).

Optimization of PEG-*b*-PPS-ss-DP polymer for plasmid DNA binding capability

PEG-b-PPS-ss-DP/plasmid DNA nanocomplexes formed at a 60:1 polymer-to-plasmid ratio optimally bind to pDNA and form stable nanostructures

To investigate the ability of the polymers to bind and condense pDNA, we next examined the formation and stability of PPDP/pDNA nanocomplexes using an electrophoretic mobility shift assay (EMSA). In this assay, the DNA will remain in the well of the gel if the PPDP/pDNA nanocomplex is stable once an electric field is applied to commence electrophoresis. On the other hand, if the nanocomplex is unstable, the unbound pDNA will migrate down the agarose gel toward the positive electrode in the presence of the electric field. These studies employed both small (S-pDNA, 4.6 kb) and large (L-pDNA, 11.7 kb) plasmids to understand whether or not different plasmid sizes required different polymer-to-plasmid ratios to perform optimally. The PPDP/pDNA complexes were formulated by combining PPDP with pDNA at various polymer-to-pDNA weight ratios (PPDP:pDNA = 1:1–120:1) for EMSA experiments (Figures 4A, 4B, and S6).

The migration of pDNA was completely obstructed by PPDP nanostructures having a polymer/pDNA weight ratio greater than 15:1 (Figures 4A and 4B). Although the amount of free or unprotected pDNA can be determined by the fluorescence intensity of GelRed dye (Chen et al., 2016), high-density packing of pDNA can result in fluorescence quenching (Kwok et al., 2016). Notably, the fluorescence of pDNA in response to binding the GelRed® nucleic acid stain progressively decreased with increasing polymer/pDNA ratio, suggesting enhanced pDNA binding for a more compact nanostructure in response to increased relative amounts of copolymer (Figures 4A and 4B). This is further validated by the observation that the dye remained in the well and did not traverse the gel during electrophoresis (Figure S6C). These results verify that PPDP polymer is capable of binding to S-pDNA (Figure 4A) and L-pDNA (Figure 4B). Of

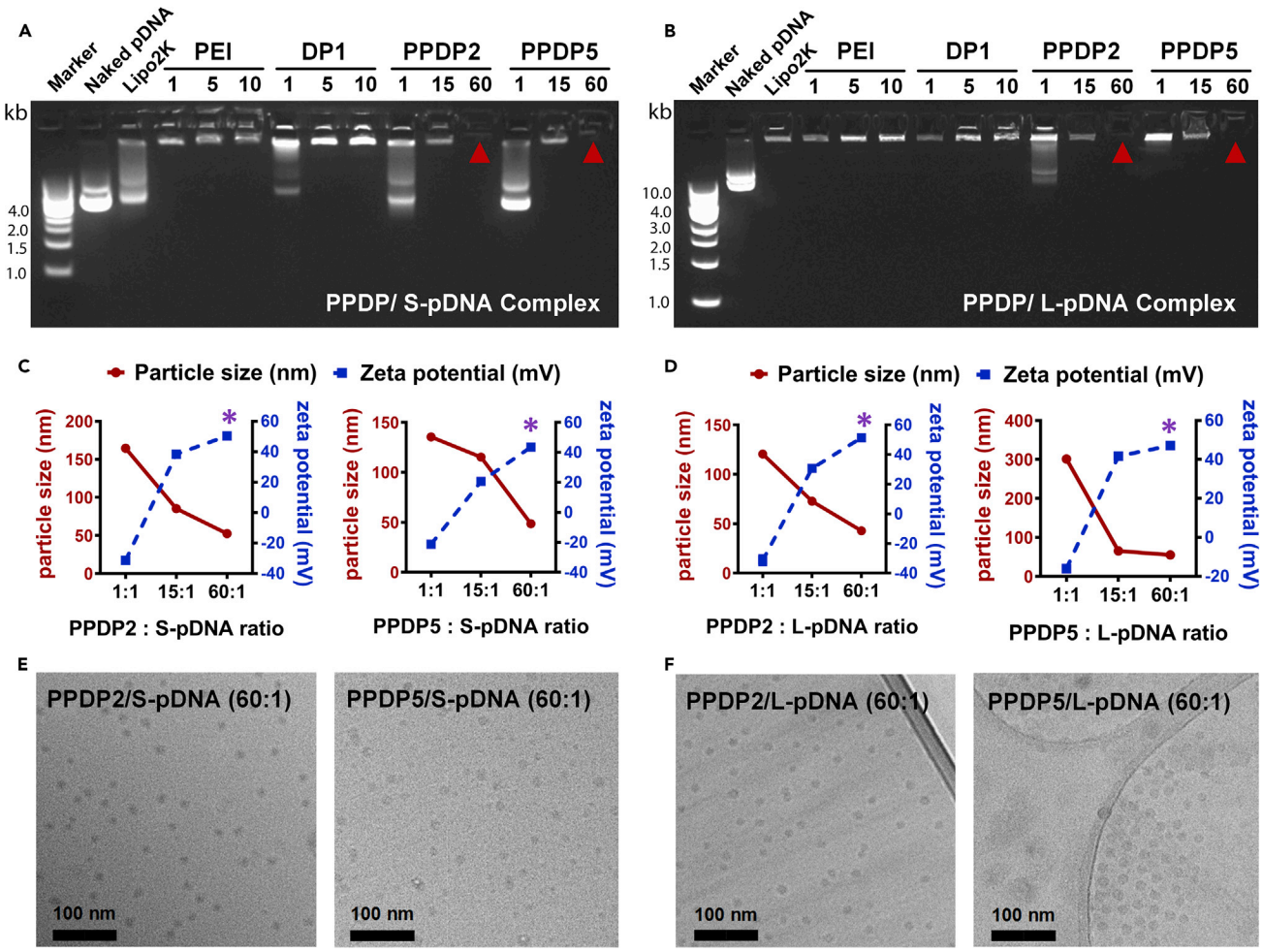

Figure 4. Optimization of PPDP/pDNA nanovectors for enhanced DNA binding capability

Electrophoretic mobility shift assay (EMSA) of PPDP/pDNA nanocomplexes with different polymer to pDNA ratios from 1:1 to 60:1. Naked pDNA, Lipofectamine 2000/pDNA complexes (Lipo2K), PEI/pDNA complexes (PEI with the molecular weight of 25 kDa), and dendritic peptide (DP1)/pDNA complexes were included as control groups. PPDP formulations were optimized by complexing with (a) S-pDNA and (b) L-pDNA. (red triangle points to PPDP/pDNA nanocomplexes that quenched the GelRed® nucleic acid stain). Effect of the mass ratio of (c) PPDP2:S-pDNA and PPDP5:S-pDNA and, (d) PPDP2:L-pDNA and PPDP5:L-pDNA on the nanocomplex particle size (red) and zeta potential (blue). Asterisks indicate the optimal PPDP:pDNA ratio. Data are presented as the mean ± SD (n = 3). e,f) Representative Cryo-TEM micrographs of the optimal PPDP/pDNA nanocomplexes. Scale bar = 100 nm.

note, PPDP2/pDNA and PPDP5/pDNA showed the lowest pDNA fluorescent intensity at the weight ratio of 60:1 (PPDP: both S-pDNA and L-pDNA) in the wells, indicating an optimal pDNA binding and compaction.

Next, we examined the effect of the mass ratio of PPDP polymer to pDNA on the particle size and zeta potential (Figures 4C and 4D). As this ratio increased, the size of the nanocomplex increased and the zeta potential became more positive (Figures 4C and 4D). Nanocomplexes ranged from negative, to neutral, to positively charged as the PPDP/pDNA ratio was increased from 1:1 to 60:1. Based on the EMSA results (Figures 4A and 4B), size and zeta potential characterization (Figures 4C and 4D), and cytotoxicity studies (Figure 3), we selected the optimal ratio of 60:1 for further gene transfection studies. When containing either S-pDNA or L-pDNA, 60:1 PPDP/pDNA nanocomplexes were observed to be spherical and monodisperse nanostructures, as observed by cryogenic transmission electron microscopy (cryoTEM) (Figures 4E, 4F and S7). The diameter and zeta potential are presented in Table S3. The PPDP system uses both self-assembly and electrostatic complexation simultaneously. A high polymer to payload ratio is standard for self-assembling systems, but high ratios are required for DNA/polymer complexes. PPDP is between these two, as it requires a higher amount of polymer so that the PPDP influences the assembly of the complexes, which may explain the uniformity of the nanostructures (Figure 4E).

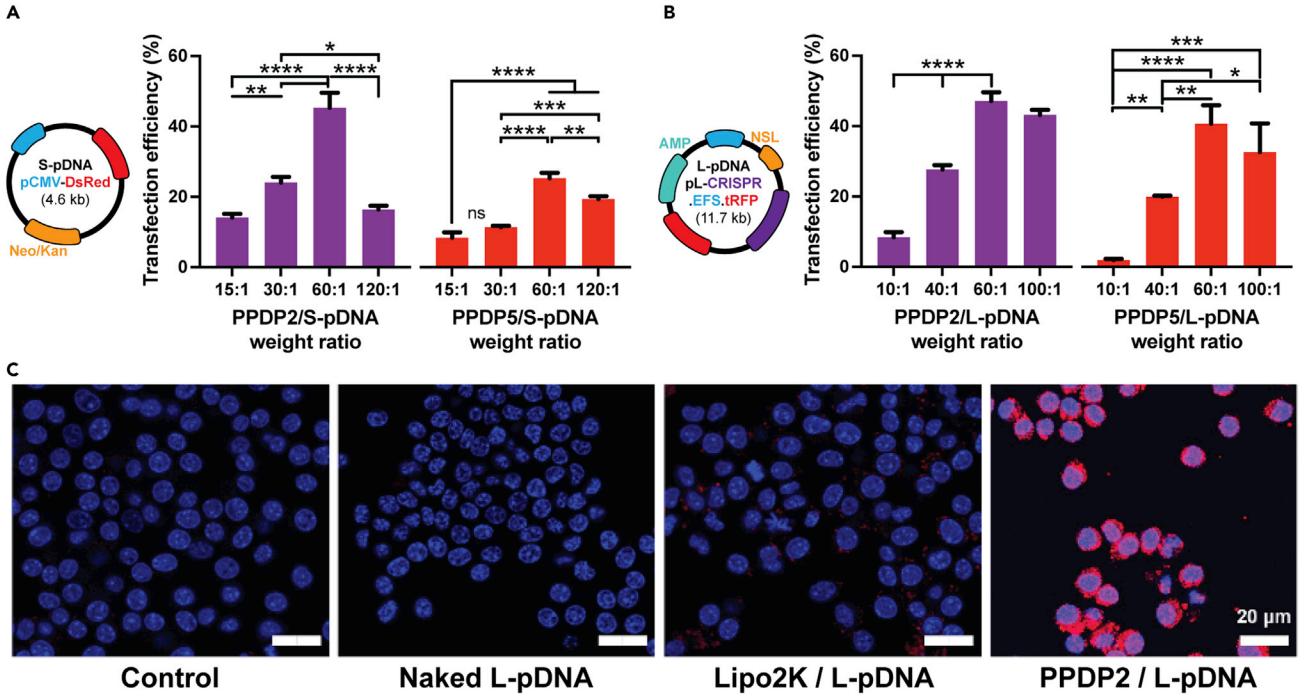

Figure 5. The 60:1 PPDP:p-DNA ratio was optimal for the transfection of macrophages with both small and large plasmids

The transfection efficiency in RAW 264.7 macrophages was determined by flow cytometry using PPDP2 (purple bar plots) or PPDP5 (red bar plots) complexed with (a) the small model plasmid (S-pDNA; pCMV-DsRed, 4.6 kb), or (b) the large model plasmid (L-pDNA; pL-CRISPR.EFS.tRFP, 11.7 kb) at the specified PPDP:pDNA ratios. Data are presented as the mean ± SD (n = 3). Significant differences were determined by ANOVA with *post hoc* Tukey's multiple comparisons test (5% significance level). *$p < 0.05$, **$p < 0.005$, ***$p < 0.001$, ****$p < 0.0001$. (c) Representative confocal image of reporter gene expression by macrophages transfected with PPDP2/L-pDNA (60:1) or Lipo2K/L-pDNA. Cellular background (control) and cells transfected with naked L-pDNA are also presented. Scale bar = 20 µm.

The 60:1 PEG-b-PPS-ss-DP:plasmid DNA ratio achieves optimal transfection efficiencies in vitro

We next examined the relationship between the PPDP:pDNA ratio and cellular transfection performance using the highest performing PPDP2 and PPDP5 constructs. We hypothesized that the 60:1 PPDP:pDNA ratio would also perform optimally in these studies as it demonstrated the most stable binding to plasmid in the EMSA studies. Furthermore, we also examined whether less economical PPDP:pDNA ratios exceeding 60:1 would provide any performance benefits at the cost of requiring additional copolymer in the formulation. Macrophages were transfected with PPDP:pDNA complexes, and the transfection efficiency (Figures 5A and 5B) and expression level of the plasmid-encoded reporter proteins (Figure S8) were quantified by flow cytometry.

For both PPDP2 and PPDP5, the highest transfection efficiencies were observed for nanovectors prepared at the 60:1 PPDP:pDNA ratio for both small (Figure 5A) and large (Figure 5B) model plasmids. With exception to the PPDP2/L-pDNA results, the 60:1 ratio performed significantly better than all other PPDP:pDNA ratios tested (Figures 5A and 5B). In the case of the exception, we note that the PPDP2-mediated transfection of the large L-pDNA plasmid was more efficient at a 60:1 ratio than a higher 100:1 ratio, although this difference was not statistically significant (Figure 5B). Nevertheless, these results demonstrate that the 60:1 PPDP:pDNA ratio is optimal for transfection with both small and large plasmids, and there is no benefit to increasing the amount of polymer used relative to the pDNA. Confocal laser scanning microscopy (CLSM) further confirmed that the level of RFP protein expression in macrophages transfected with L-pDNA using PPDP2 was greater than the RFP expression level achieved by Lipo2K (Figure 5C).

PEG-*b*-PPS-ss-DP undergoes a disorder-to-order transition into a helical conformation under acidic conditions and promotes the intracellular release of plasmid DNA cargo

The dendritic peptide conjugate of PEG-b-PPS-ss-DP nanovectors adopt a helical conformation under pH 6.0

The results of our preliminary screening and polymer-to-DNA ratio optimization studies demonstrated that PPDP2 prepared at a 60:1 PPDP:pDNA consistently outperformed all other nanovectors and commercial

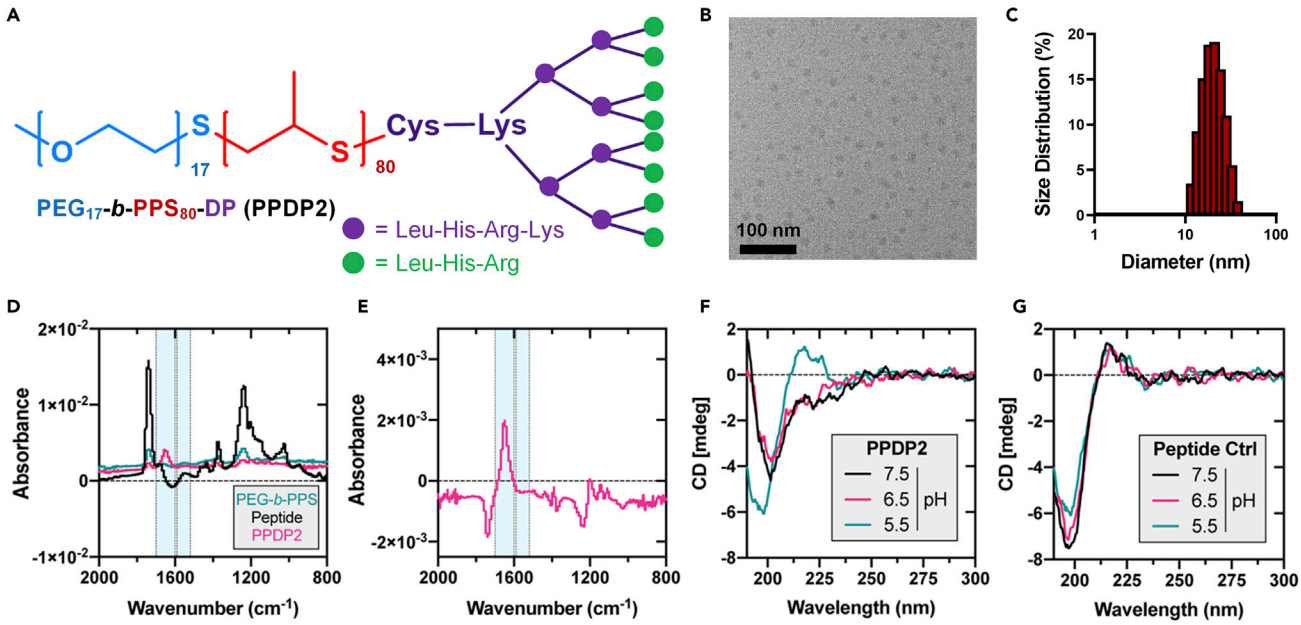

Figure 6. Structural characterization of PPDP

(A) Schematic illustration depicting the amino acid composition of the PPDP polymer (PEG_m-*b*-PPS_n-ss-DP).

(B and C) Representative Cryo-TEM micrograph (scale bar = 100 nm) and (c) size distribution of PPDP2 determined by DLS.

(D) FT-IR spectra of PEG-*b*-PPS (green), dendritic peptide (black), and PPDP2 (pink). The regions highlighted in blue correspond to the amide I (1700–1600 cm^{-1}) and amide II (1590–1520 cm^{-1}) bands.

(E and F) PPDP2 spectra with PEG-*b*-PPS contributions subtracted. Circular dichroism (CD) spectroscopy analysis of DP secondary structure in (f) assembled PPDP2 nanostructures or in (g) free form (i.e. unconjugated peptide control). Suspensions were adjusted to pH 7.5, 6.5, or 5.5, as specified in the plot legends.

reagents. Thus, this PPDP2 formulation was investigated further in mechanistic studies seeking to characterize its endolysosomal escape properties. Based on the biochemical properties of the DP amino acid composition (Figure 6A), we hypothesized that the conformation of this peptide would change in increasingly acidic environments.

To assess the pH-responsive structure of PPDP, spherical nanostructures were self-assembled from PPDP2 copolymer (Figure 6B), which demonstrated a mean diameter of 19.9 nm and surface charge of 48.0 mV as measured by DLS (Figure 6C). The DP component of the PPDP2 nanostructures is readily detectable by Fourier transform infrared (FTIR) spectroscopy in solution (Figures 6D and 6E). PPDP2 nanostructures exhibited the expected amide I peak in the 1700–1600 cm^{-1} band (C=O stretching), which is characteristic of peptide bonds (Figure 6D). As expected, this peak was also detectable in the DP peptide control, although its intensity was partially masked by a stronger peak in the 1800–1700 cm^{-1} band. Subtracting the PEG-*b*-PPS spectra from that of the PPDP2 sample enables a preliminary assessment of the helical secondary structure. In the difference spectra presented in Figure 6E, a strong peak is observed near 1660 cm^{-1} within the amide I band. These results suggested that PPDP2 may adopt a helical secondary structure.

We next performed circular dichroism (CD) spectroscopy to more thoroughly examine if the DP adopts a helical secondary structure and whether a conformational change occurs in response to a shift from pH 7.5 to pH 5.5 (Figures 6F, 6G, and S9). This pH range is particularly interesting in the context of a nanostructure trafficking through the endolysosomal pathway that becomes progressively more acidic. In our biophysical studies, PPDP2 did not take on a traditional alpha-helix secondary structure under any condition, which would be indicated by two negative peaks at 208 and 222 nm in a CD spectrum (Provencher and Glöckner, 1981) (Figure 6F).

We initially suspected that PPDP2 is intrinsically disordered, which is a ubiquitous feature of many peptides and proteins (Uversky et al., 2000, 2005; Dunker et al., 2001; Linding et al., 2004; Oates et al., 2012; Vincent

and Schnell, 2016, 2019; Vincent et al., 2016, 2019; Wang et al., 2016). Closer inspection of the PPDP2 CD spectra instead provides evidence of a different, more esoteric, type of helical structure resembling that of PPII (polyproline II)-like structures, which can be formed by peptides lacking proline residues (Kumar and Bansal, 2016) and have a characteristic combination of spectral features of disordered and ordered states (Figure 6F). Proteins and peptides adopting a random coil state commonly have a negative peak near 200 nm. However, a PPII-like helical structure is revealed by a characteristic positive peak near 220 nm (Lopes et al., 2014) (but as low as 210 nm for proline-lacking peptides adopting a PPII-like conformation (Lella and Mahalakshmi, 2017)) and minima at 197 nm (Lella and Mahalakshmi, 2017), which is a spectral signature that is used to distinguish these special helical conformations from purely disordered states. In our studies, PPDP2 exhibited a strong negative peak at ~201 nm at pH 7.5 and at ~204 nm at pH 6.5, whereas the most acidic conditions (pH 5.5) induced a strong leftward shift to a minimum at ~197 nm. The key feature that distinguishes the PPDP2 CD spectra from a disordered spectrum is observed at pH 5.5, where a strong positive peak is observed at 215 nm (Figure 6F). Thus, the PPDP2 CD spectrum contains both a negative peak at 197 nm and a positive peak at 215 nm under conditions that mimic a more strongly acidic intracellular environment, suggesting that it adopts a PPII-like helical conformation below pH 6.5. This interpretation is consistent with past studies that demonstrate lysine homopolymers adopt PPII-like helical structures with similar spectral features (Rucker and Creamer, 2002; Tiffany and Krimm, 1968, 1972), which can be stabilized by either the conformation of lysine in the backbone (Rucker and Creamer, 2002) or by electrostatic interactions (Arunkumar et al., 1997). As the lysine side chains within the DP are employed for branching (Figure 1) and thus not available for electrostatic interactions, the chemical bonding of lysine residues within the DP backbone likely promotes the formation of a PPII-like helical conformation.

Interestingly, the free DP (unconjugated control) exhibits a peak at ~195 nm at pH 7.5 and pH 6.5, and a peak at ~200 nm at pH 5.5 (Figure 6G). Unconjugated DPs also exhibita positive peak (~215 nm) at all pH values, suggesting that it has a PPII-like helical structure under all conditions tested. As the positive peak is only observed at a pH 5.5 for PPDP2, these results suggest that conjugating the peptide to the polymer rendered the peptide conformation pH-responsive. In the context of a gene delivery technology, the absence of the ~215 nm positive peak at pH 7.5 and pH 6.5 in the PPDP2 CD spectra suggest the peptide is disordered prior to reaching the acidic lysosomal compartment. Yet, once PPDP2 reaches the lysosome (pH < 6), it can adopt a helical conformation. This PPDP2 disorder-to-order transition that occurs in acidic environments may provide a mechanism for lysosomal escape. At all pH values examined, the ionizable guanidino group of arginine (pKa ~9) in PPDP2 is protonated and provides a stable electrostatic interaction with DNA. At a pH below 6.0, the imidazole group (pKa ~6) of histidine residues should be protonated and provide an additional means for electrostatic interaction with DNA. Stabilizing the PPDP2-DNA interaction within acid lysosomal compartments is important, as the higher order nanostructure disassembles under these conditions owing to the oxidation of PPS (Vasdekis et al., 2012). Furthermore, the protonated histidine residues are also known to facilitate membrane disruption in concert with leucine residues that play a role in membrane binding (Erazo-Oliveras et al., 2012; Summerton, 2005). Consequently, the oxidation-mediated loss in PPS hydrophobicity as well as the enhancement in DNA-binding and membrane-disruption capabilities of the DP under acidic conditions, all coincide with the adoption of a PPII-like helix within the lysosome. Of note, helical conformations are known to promote the cytoplasmic release of cargo from lysosomal compartments (El-Sayed et al., 2009; Ohmori et al., 1997). Thus, we conclude that the formation of helical structures acts synergistically with the functionality of the ionized amino acid residues and the oxidized PPS moieties of PPDP2 at low pH (pH < 6) to promote the efficient lysosomal release of DNA cargo into the cytoplasm.

PEG-b-PPS-ss-DP traffics through the endolysosomal pathway and releases plasmid DNA payloads into the cytoplasm in a time-dependent fashion

We sought to investigate the cellular internalization and localization of DNA cargo delivered using the pH-responsive PPDP2 nanovector. To this end, CLSM imaging was used to visualize the intracellular trafficking of PPDP2/Alexa Fluor 488-lableled pDNA (pcDNA3.1, 5.4 kb) nanocomplexes at different timepoints. Early 1 and 4 h timepoints were included to examine nanovector migration through the endolysosomal pathway, as well as the onset of endosomal escape, whereas an 18 h timepoint was included to examine changes in the cytoplasmic accumulation of the pDNA payload with time (Figure 7). After 1 h incubation with RAW264.7 macrophages, the green fluorescence (Alexa Fluor 488) was predominantly observed as puncta that co-localized with endosomal/lysosomal compartments. At longer incubation times of 4 and 18 h,

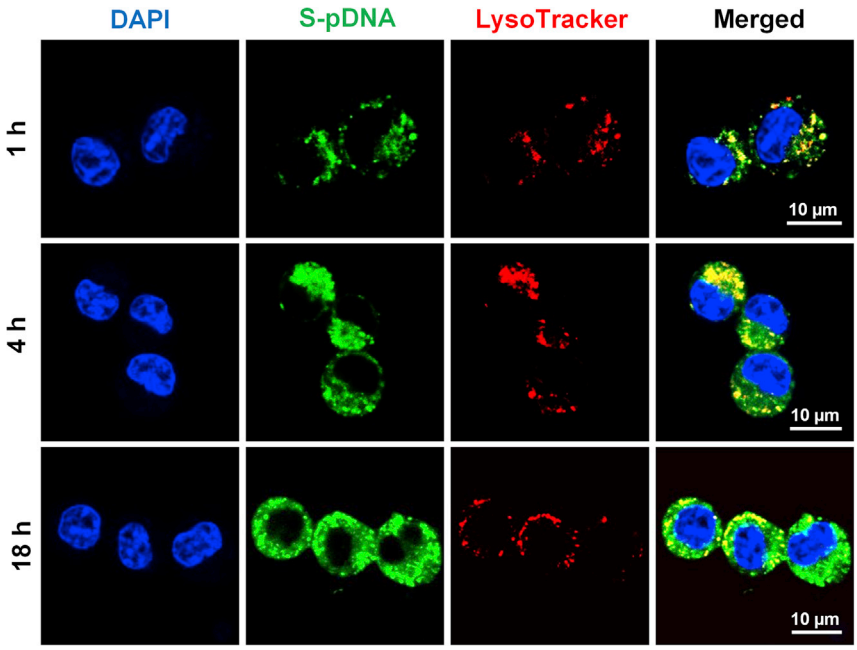

Figure 7. Endosomal escape and cytosolic delivery of PPDP2/pDNA complexes in RAW 264.7 macrophages

RAW 264.7 macrophages were incubated with PPDP2/AF488-labeled S-pDNA (pcDNA3.1, 5.4 kb) nanocomplexes formed using a PPDP2 to pDNA weight ratio of 60:1. Representative confocal images display PPDP2/S-pDNA complexes within cells after 1, 4, and 18 h incubation periods. LysoTracker red was used to label late endosomes/lysosomes. Nuclei were stained with DAPI (blue). Co-localization of green plasmid DNA and red endo/lysosomes appears as yellow in the images. Scale bar = 10 µm.

nanocomplexes escaped from endolysosomal compartments and were released into the cytosol. Cytoplasmic release is observed by the presence of diffuse green fluorescence that no longer colocalizes with the endosomal/lysosomal compartments. A fraction of the nanocomplexes were still entrapped within endosomal/lysosomal compartments at the 4 and 18 h timepoints. However, the diffuse green signal was much greater in intensity at 18 h compared to 4 h, and this change also coincided with a decrease in the co-localization signal at 18 h. These results demonstrate that Alexa Fluor 488-lableled pDNA efficiently and increasingly escaped from the lysosome over time following intracellular delivery via PPDP2 nanocomplexes.

The PEG-*b*-PPS-ss-DP platform efficiently transfects both innate and adaptive immune cells

To verify the broad applicability of PPDP2 and PPDP5 as potential DNA delivery vectors, we assessed the L-pDNA transfection of diverse cell lines (Figure 8). Transfection was performed under the standard culture conditions for each cell type in the presence of serum. We first tested NIH 3T3 mouse fibroblast cells, which have been widely used for DNA transfection studies and recombinant protein expression in biological research. Confocal imaging revealed extensive RFP fluorescence expression after 48 h in NIH3T3cells that were transfected by PPDP2/L-pDNA, but minimal to no detectable signal for Naked L-pDNA and Lipo2K/L-pDNA at the same timepoint (Figure 8A). Flow cytometry analysis demonstrated that PPDP2 and PPDP5 exhibited transfection efficiencies of 69.6 and 57.5%, respectively, in fibroblasts (Figure 8B). These transfection efficiencies were significantly greater than the 12% transfection efficiency determined for Lipo2K (Figure 8B). Consistent with our results in macrophages, PPDP2 transfected fibroblasts with an efficiency that was significantly greater than that of PPDP5 (Figure 8B).

We next examined whether the PPDP technologies could efficiently transfect dendritic cells (DCs). Developing technologies to facilitate the production of genetically engineered DCs is of great interest owing to their unique and versatile role in immune regulation and their potential use in creating next-generation vaccines for cancer and infectious disease. However, the genetic manipulation of primary DCs remains challenging and continues to obstruct progress in developing DC-based therapies. Primary mouse bone

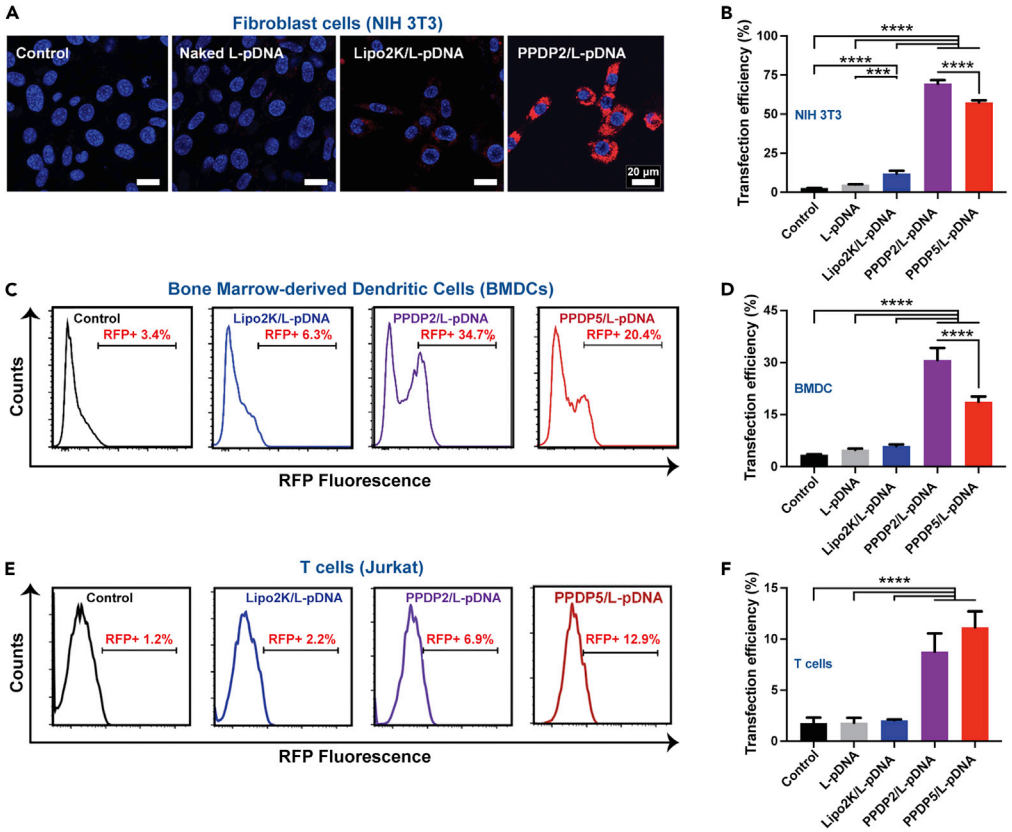

Figure 8. Transfection of PPDP/L-pDNA nanovector in fibroblasts, dendritic cells, and T cells

NIH 3T3, BMDC, and Jurkat T cells were transfected with L-pDNA (pL-CRISPR.EFS.tRFP, 11.7 kb) using PPDP2 and PPDP5 nanovectors with the PPDP to pDNA weight ratio of 60:1.

(A) Representative confocal image of PPDP2/L-pDNA complexes demonstrated the transfection of L-pDNA after cellular uptake. Scale bar = 20 μm.

(B) Transfection efficiency for NIH3T3 cells.

(C and D) Flow cytometry histogram and (d) the percentage of transfected cells in BMDCs.

(E and F) Flow cytometry histogram and (f) the percentage of transfected Jurkat T cells. Naked pDNA and Lipo2K/pDNA complexes (Lipo2K) were included as negative and positive controls, respectively. Data are presented as the mean ± SD (n = 3–4). Significance was determined by ANOVA with *post hoc* Tukey's multiple comparisons test (5% significance level). ***$p < 0.001$, ****$p < 0.0001$.

marrow-derived dendritic cells (BMDCs) were transfected with L-pDNA using PPDP2 and PPDP5 (Figures 8C and 8D). PPDP2-mediated transfection resulted in 30.7% RFP positive (RFP+) cells, whereas 18.7% of cells were RFP + after transfection with PPDP5 (Figures 8C and 8D). These percentages were significantly greater than both naked pDNA and Lipo2K controls (Figures 8C and 8D).

Lastly, we investigated the use of PPDP2 and PPDP5 for transfecting Jurkat T cells with a large plasmid (Figures 8E and 8F). Jurkat T cells are immortalized human T lymphocytes that are commonly employed to study T cell biology and for developing prototypes of engineered T cell technologies. PPDP2 and PPDP5 increased the percentage of RFP + T cells, as observed by the rightward shift in flow cytometry histograms compared to the negative control group (Figure 8E). Interestingly, both PPDP2 and PPDP5 achieved transfection efficiencies that were significantly greater than that achieved by Lipo2K (Figure 8F). Although PPDP5 transfected T cells with large plasmids slightly more efficiently than PPDP2, this difference in transfection was not significantly different (Figure 8F). This trend observed for T cells (Figure 8F) differs from our observations using fibroblasts and DCs, where PPDP2 achieved transfection efficiencies that were significantly greater than PPDP5 (Figures 8B–8D). It is unclear why PPDP2 was not also superior for transfecting T cells with large plasmids; however, understanding the mechanism for this difference is outside the scope of the present work. Collectively, these results demonstrate that PPDP2 and PPDP5 dramatically improve

the delivery of large pDNA molecules to primary immune cells and achieve greater transfection efficiencies than commercially available transfection reagents (Figure 8).

The advantages of forming nanovectors using the controlled self-assembly of PEG-*b*-PPS block copolymers may explain the observed lowered toxicity and improved transfection efficiency compared to Lipo2K. First, as evidenced by both SAXS (Figure S3 and Table S2) and CryoTEM (Figure 4), PPDP forms highly uniform spherical structures that are indicative of PEG-*b*-PPS copolymer self-assembly (Allen et al., 2017, 2018a). Such nanostructures are maintained by the balance between aggregated hydrophobic PPS domains and highly dense PEG corona, the former enhancing the stability of the assembly while the latter minimizes nonspecific cellular and protein interactions (Cerritelli et al., 2009a). These properties could inhibit interactions between the cationic DP and cell membranes that likely resulted in the observed toxicity for the DP in the absence of PEG-*b*-PPS (Figure 3). Furthermore, all transfection experiments in our study were performed in a medium with serum and growth factors beneficial for culturing primary cells. Previous studies have demonstrated that the transfection efficiency of lipofectamine decreases dramatically in the medium with serum (Yang and Huang, 1997). Interactions of cationic lipids with serum proteins significantly decrease the colloidal stability of Lipo2K-DNA complexes, resulting in aggregation and sedimentation. The dense PEG corona of self-assembled PEG-*b*-PPS nanostructures could improve the stability of nanocomplexes, decrease their aggregation and reduce the interaction with proteins. Moreover, functional groups in PPDP, such as leucine and histidine residues, and bioreducible disulfide bond between PPS and DP could facilitate pDNA escape from endolysosomal compartments for more efficient access to the nucleus. All of these factors could contribute to the PPDP polymer being a more efficient gene delivery platform compared to Lipo2K.

Conclusions

We developed and optimized a polymeric nanovector as a non-viral and non-toxic plasmid transfection reagent for diverse immune cell types without the need for specialized culture conditions or medium. The PPDP vehicle consists of a self-assembling PEG-*b*-PPS copolymer conjugated to a cationic DP. Each branch of the DP possesses a terminal arginine for stable complexation with DNA via electrostatic interactions, and the lysine-branched backbone undergoes a helical conformational change in acidic environments that may assist with endosomal escape. This lysosomal escape is a prerequisite for pDNA diffusion into the nucleus where it can be transcribed and translated into a protein product and is thus an essential feature of any effective gene delivery technology and transfection reagent. Nanocarriers assembled from PEG-*b*-PPS copolymers have previously demonstrated enhanced cytosolic delivery of diverse therapeutic payloads (Dowling et al., 2017; Scott et al., 2012; Yi et al., 2019), and here the conjugation of a cationic DP achieves this capability for both small (S-pDNA; 4.6 kb) and large (L-pDNA; 11.7 kb). Screening the size and surface character of PPDP yielded the PPDP2 and PPDP5 constructs, which were found to be optimal for enhanced transfection with significantly less toxicity than the commercial standard lipofectamine in studies using macrophages, fibroblasts, primary BMDCs, and T cells *in vitro*. Although PPDP2 was found to be the more efficient overall, both constructs were particularly useful for transfecting cells with large pDNA elements. PPDP is, therefore, a promising non-viral vector with numerous advantages for efficient *in vitro* transfection, including exceptionally low toxicity, proficient cytosolic delivery of large genetic elements, and efficacy under standard culture conditions for typically difficult to transfect immune cell populations.

Limitations of the study

In this study, we optimized a self-assembling block copolymer linked to a cationic dendritic peptide (DP) to form monodisperse spherical complexes with small and large plasmids. These nanovectors efficiently transfected diverse immune cell populations *in vitro* with minimal toxicity and without the need for specialized serum-free medium. Future efforts will further develop this delivery platform for other nucleic acid constructs as well as optimize *in vivo* transfection.

STAR★METHODS

Detailed methods are provided in the online version of this paper and include the following:

- KEY RESOURCES TABLE
- RESOURCE AVAILABILITY
  - Lead contact
  - Materials availability

SUPPLEMENTAL INFORMATION

Supplemental information can be found online at https://doi.org/10.1016/j.isci.2022.104555.

ACKNOWLEDGMENTS

S.Y. and S.-Y. K. contributed equally to this work. This work was supported by the National Institutes of Health (no. 1DP2HL132390-01 and 5R01AI145345-04) and the National Research Foundation of Korea (NRF) grant funded by the Korea government (MSIT) (No. 2021R1C1C2003091). M.P.V. gratefully acknowledges support from the Ryan Fellowship, the International Institute for Nanotechnology at Northwestern University, and the Northwestern University Multidisciplinary Visual Sciences Training Program (T32 Fellowship funded by NEI Award 2T32EY025202-06). The authors would like to thank Dr. Eric W. Roth for CryoTEM assistance. This work made use of the BioCryo facility of Northwestern University's NUANCE center, which has received support from the Soft and Hybrid Nanotechnology Experimental (SHyNE) Resource (NSF ECCS-1542205); the MRSEC program (NSF DMR-1720139) at the Materials Research Center; the International Institute for Nanotechnology (IIN); and the State of Illinois, through the IIN. It also made use of the CryoCluster equipment, which has received support from the MRI program (NSFDMR-1229693).

AUTHOR CONTRIBUTIONS

S.Y., S.Y.K., M.P.V., and E.A.S. contributed to the conceptualization of the study, data analysis, and wrote the article. S.Y. and F.D. contributed to the polymer synthesis. S.Y., S.-\Y. K, M.P.V., and S.B. contributed to the characterization of nanostructure morphology. M.P.V. contributed to the characterization of stimuli-responsive changes in peptide conformation. S.Y., S.Y.K, S.A.Y and M.P.V. contributed to the cell work and supporting analyses. M.P.V. contributed to the statistical analysis.

DECLARATION OF INTERESTS

The authors declare no competing interests.

Received: December 23, 2021
Revised: April 29, 2022
Accepted: June 2, 2022
Published: July 15, 2022

REFERENCES

Abbasi, E., Aval, S.F., Akbarzadeh, A., Milani, M., Nasrabadi, H.T., Joo, S.W., Hanifehpour, Y., Nejati-Koshki, K., and Pashaei-Asl, R. (2014). Dendrimers: synthesis, applications, and properties. Nanoscale Res. Lett. *9*, 247. https://doi.org/10.1186/1556-276X-9-247.

Allen, S., Osorio, O., Liu, Y.-G., and Scott, E. (2017). Facile assembly and loading of theranostic polymersomes via multi-impingement flash nanoprecipitation. J. Control. Release *262*, 91–103. https://doi.org/10.1016/j.jconrel.2017.07.026.

Allen, S., Vincent, M., and Scott, E. (2018a). Rapid, scalable assembly and loading of bioactive proteins and immunostimulants into diverse synthetic nanocarriers via flash nanoprecipitation. J. Vis. Exp. 57793. https://doi.org/10.3791/57793.

Allen, S.D., Liu, Y.-G., Bobbala, S., Cai, L., Hecker, P.I., Temel, R., and Scott, E.A. (2018b). Polymersomes scalably fabricated via flash nanoprecipitation are non-toxic in non-human primates and associate with leukocytes in the spleen and kidney following intravenous

administration. Nano Res. *11*, 5689–5703. https://doi.org/10.1007/s12274-018-2069-x.

Arunkumar, A.I., Kumar, T.K., and Yu, C. (1997). Non-specific helix-induction in charged homopolypeptides by alcohols. Biochim. Biophys. Acta *1338*, 69–76. https://doi.org/10.1016/s0167-4838(96)00191-4.

Ayuso, E. (2016). Manufacturing of recombinant adeno-associated viral vectors: new technologies are welcome. Mol. Ther. Methods Clin. Dev. *3*, 15049. https://doi.org/10.1038/mtm.2015.49.

Baldo, A., van den Akker, E., Bergmans, H.E., Lim, F., and Pauwels, K. (2013). General considerations on the biosafety of virus-derived vectors used in gene therapy and vaccination. Curr. Gene Ther. *13*, 385–394. https://doi.org/10.2174/15665232113136660005.

Bobbala, S., Allen, S.D., Yi, S., Vincent, M., Frey, M., Karabin, N.B., and Scott, E.A. (2020). Employing bicontinuous-to-micellar transitions in nanostructure morphology for on-demand photo-oxidation responsive cytosolic delivery and off–on cytotoxicity. Nanoscale *12*, 5332–5340. https://doi.org/10.1039/C9NR10921H.

Bobbala, S., Vincent, M.P., and Scott, E.A. (2021). Just add water: hydratable, morphologically diverse nanocarrier powders for targeted delivery. Nanoscale *13*, 11349–11359. https://doi.org/10.1039/D1NR02188E.

Boussif, O., Lezoualc'h, F., Zanta, M.A., Mergny, M.D., Scherman, D., Demeneix, B., and Behr, J.P. (1995). A versatile vector for gene and oligonucleotide transfer into cells in culture and in vivo: polyethylenimine. Proc. Natl. Acad. Sci. U S A. *92*, 7297–7301. https://doi.org/10.1073/pnas.92.16.7297.

Cerritelli, S., Velluto, D., and Hubbell, J.A. (2007). PEG-SS-PPS: reduction-sensitive disulfide block copolymer vesicles for intracellular drug delivery. Biomacromolecules *8*, 1966–1972. https://doi.org/10.1021/bm070085x.

Cerritelli, S., O'Neil, C.P., Velluto, D., Fontana, A., Adrian, M., Dubochet, J., and Hubbell, J.A. (2009a). Aggregation behavior of poly(ethylene glycol-bl-propylene sulfide) di- and triblock copolymers in aqueous solution. Langmuir *25*, 11328–11335. https://doi.org/10.1021/la900649m.

Cerritelli, S., O'Neil, C.P., Velluto, D., Fontana, A., Adrian, M., Dubochet, J., and Hubbell, J.A. (2009b). Aggregation behavior of poly(ethylene glycol-bl-propylene sulfide) di- and triblock copolymers in aqueous solution. Langmuir *25*, 11328–11335. https://doi.org/10.1021/la900649m.

Chang, S., Mahon, E.L., MacKay, H.A., Rottmann, W.H., Strauss, S.H., Pijut, P.M., Powell, W.A., Coffey, V., Lu, H., Mansfield, S.D., and Jones, T.J. (2018). Genetic engineering of trees: progress and new horizons. In Vitro Cell. Dev.Biol. Plant *54*, 341–376. https://doi.org/10.1007/s11627-018-9914-1.

Chen, Y., Li, Y., Gao, J., Cao, Z., Jiang, Q., Liu, J., and Jiang, Z. (2016). Enzymatic PEGylated poly(lactone-co-β-amino ester) nanoparticles as biodegradable, biocompatible and stable vectors for gene delivery. ACS Appl. Mater. Interfaces *8*, 490–501. https://doi.org/10.1021/acsami.5b09437.

Cong, L., and Zhang, F. (2015). Genome engineering using CRISPR-Cas9 system. Methods Mol. Biol. *1239*, 197–217. https://doi.org/10.1007/978-1-4939-1862-1_10.

Cornu, T.I., Mussolino, C., and Cathomen, T. (2017). Refining strategies to translate genome editing to the clinic. Nat. Med. *23*, 415–423. https://doi.org/10.1038/nm.4313.

David, R.M., and Doherty, A.T. (2017). Viral vectors: the road to reducing genotoxicity. Toxicol. Sci. *155*, 315–325. https://doi.org/10.1093/toxsci/kfw220.

Dowling, D.J., Scott, E.A., Scheid, A., Bergelson, I., Joshi, S., Pietrasanta, C., Brightman, S., Sanchez-Schmitz, G., Van Haren, S.D., Ninković, J., et al. (2017). Toll-like receptor 8 agonist nanoparticles mimic immunomodulating effects of the live BCG vaccine and enhance neonatal innate and adaptive immune responses. J. Allergy Clin. Immunol. *140*, 1339–1350. https://doi.org/10.1016/j.jaci.2016.12.985.

Dunbar, C.E., High, K.A., Joung, J.K., Kohn, D.B., Ozawa, K., and Sadelain, M. (2018). Gene therapy comes of age. Science *359*, eaan4672. https://doi.org/10.1126/science.aan4672.

Dunker, A.K., Lawson, J.D., Brown, C.J., Williams, R.M., Romero, P., Oh, J.S., Oldfield, C.J., Campen, A.M., Ratliff, C.M., Hipps, K.W., et al. (2001). Intrinsically disordered protein. J. Mol. Graph. Model. *19*, 26–59. https://doi.org/10.1016/S1093-3263(00)00138-8.

El-Sayed, A., Futaki, S., and Harashima, H. (2009). Delivery of macromolecules using arginine-rich cell-penetrating peptides: ways to overcome endosomal entrapment. AAPS J. *11*, 13–22. https://doi.org/10.1208/s12248-008-9071-2.

Erazo-Oliveras, A., Muthukrishnan, N., Baker, R., Wang, T.-Y., and Pellois, J.-P. (2012). Improving the endosomal escape of cell-penetrating peptides and their cargos: strategies and challenges. Pharmaceuticals *5*, 1177–1209. https://doi.org/10.3390/ph5111177.

Fischer, D., Bieber, T., Li, Y., Elsässer, H.P., and Kissel, T. (1999). A novel non-viral vector for DNA delivery based on low molecular weight, branched polyethylenimine: effect of molecular weight on transfection efficiency and cytotoxicity. Pharm. Res. *16*, 1273–1279. https://doi.org/10.1023/a:1014861900478.

Godbey, W.T., Wu, K.K., and Mikos, A.G. (1999). Size matters: molecular weight affects the efficiency of poly(ethylenimine) as a gene delivery vehicle. J. Biomed. Mater. Res. *45*, 268–275. https://doi.org/10.1002/(sici)1097-4636(19990605)45:3<268::aid-jbm15>3.0.co;2-q.

Goswami, R., Subramanian, G., Silayeva, L., Newkirk, I., Doctor, D., Chawla, K., Chattopadhyay, S., Chandra, D., Chilukuri, N., and Betapudi, V. (2019). Gene therapy leaves a vicious cycle. Front. Oncol. *9*, 297. https://doi.org/10.3389/fonc.2019.00297.

Hill, A.B., Chen, M., Chen, C.-K., Pfeifer, B.A., and Jones, C.H. (2016). Overcoming gene delivery hurdles: physiological considerations for nonviral vectors. Trends Biotechnol. *34*, 91–105. https://doi.org/10.1016/j.tibtech.2015.11.004.

Knott, G.J., and Doudna, J.A. (2018). CRISPR-Cas guides the future of genetic engineering. Science *361*, 866–869. https://doi.org/10.1126/science.aat5011.

Kumar, P., and Bansal, M. (2016). Structural and functional analyses of PolyProline-II helices in globular proteins. J. Struct. Biol. *196*, 414–425. https://doi.org/10.1016/j.jsb.2016.09.006.

Kwok, A., Eggimann, G.A., Reymond, J.-L., Darbre, T., and Hollfelder, F. (2013). Peptide dendrimer/lipid Hybrid systems are efficient DNA transfection reagents: structure–activity relationships highlight the role of charge distribution across dendrimer generations. ACS Nano *7*, 4668–4682. https://doi.org/10.1021/nn400343z.

Kwok, A., McCarthy, D., Hart, S.L., and Tagalakis, A.D. (2016). Systematic comparisons of formulations of linear oligolysine peptides with siRNA and plasmid DNA. Chem. Biol. Drug Des. *87*, 747–763. https://doi.org/10.1111/cbdd.12709.

Larocca, R.A., Abbink, P., Peron, J.P.S., de A Zanotto, P.M., Iampietro, M.J., Badamchi-Zadeh, A., Boyd, M., Ng'ang'a, D., Kirilova, M., Nityanandam, R., et al. (2016). Vaccine protection against Zika virus from Brazil. Nature *536*, 474–478. https://doi.org/10.1038/nature18952.

Lella, M., and Mahalakshmi, R. (2017). Solvation driven conformational transitions in the second transmembrane domain of mycobacteriophage holin. J. Pept. Sci. *108*. https://doi.org/10.1002/bip.22894.

Li, H., Yang, Y., Hong, W., Huang, M., Wu, M., and Zhao, X. (2020). Applications of genome editing technology in the targeted therapy of human diseases: mechanisms, advances and prospects. Signal Transduct. Target. Ther. *5*, 1. https://doi.org/10.1038/s41392-019-0089-y.

Linding, R., Schymkowitz, J., Rousseau, F., Diella, F., and Serrano, L. (2004). A comparative study of the relationship between protein structure and beta-aggregation in globular and intrinsically disordered proteins. J. Mol. Biol. *342*, 345–353. https://doi.org/10.1016/j.jmb.2004.06.088.

Liu, C., Zhang, L., Liu, H., and Cheng, K. (2017). Delivery strategies of the CRISPR-Cas9 gene-editing system for therapeutic applications. J. Control. Release *266*, 17–26. https://doi.org/10.1016/j.jconrel.2017.09.012.

Lopes, J.L.S., Miles, A.J., Whitmore, L., and Wallace, B.A. (2014). Distinct circular dichroism spectroscopic signatures of polyproline II and unordered secondary structures: applications in secondary structure analyses. Protein Sci. *23*, 1765–1772. https://doi.org/10.1002/pro.2558.

Madaan, K., Kumar, S., Poonia, N., Lather, V., and Pandita, D. (2014). Dendrimers in drug delivery and targeting: Drug-dendrimer interactions and toxicity issues. J. Pharm. BioAllied Sci. *6*, 139. https://doi.org/10.4103/0975-7406.130965.

Malik, N., Wiwattanapatapee, R., Klopsch, R., Lorenz, K., Frey, H., Weener, J.W., Meijer, E.W., Paulus, W., and Duncan, R. (2000). Dendrimers: relationship between structure and

biocompatibility in vitro, and preliminary studies on the biodistribution of 125I-labelled polyamidoamine dendrimers in vivo. J. Control. Release *65*, 133–148. https://doi.org/10.1016/s0168-3659(99)00246-1.

Moleirinho, M.G., Silva, R.J.S., Alves, P.M., Carrondo, M.J.T., and Peixoto, C. (2020). Current challenges in biotherapeutic particles manufacturing. Expert. Opin. Biol. Ther. *20*, 451–465. https://doi.org/10.1080/14712598.2020.1693541.

Napoli, A., Tirelli, N., Kilcher, G., and Hubbell, A. (2001). New synthetic methodologies for amphiphilic multiblock copolymers of ethylene glycol and propylene sulfide. Macromolecules *34*, 8913–8917. https://doi.org/10.1021/ma0108057.

Nayerossadat, N., Maedeh, T., and Ali, P.A. (2012). Viral and nonviral delivery systems for gene delivery. Adv. Biomed. Res. *1*, 27. https://doi.org/10.4103/2277-9175.98152.

Nidetz, N.F., McGee, M.C., Tse, L.V., Li, C., Cong, L., Li, Y., and Huang, W. (2020). Adeno-associated viral vector-mediated immune responses: understanding barriers to gene delivery. Pharmacol. Ther. *207*, 107453. https://doi.org/10.1016/j.pharmthera.2019.107453.

Oates, M.E., Romero, P., Ishida, T., Ghalwash, M., Mizianty, M.J., Xue, B., Dosztányi, Z., Uversky, V.N., Obradovic, Z., Kurgan, L., et al. (2012). D2P2: database of disordered protein predictions. Nucleic Acids Res. *41*, D508–D516. https://doi.org/10.1093/nar/gks1226.

Ohmori, N., Niidome, T., Wada, A., Hirayama, T., Hatakeyama, T., and Aoyagi, H. (1997). The enhancing effect of anionic alpha-helical peptide on cationic peptide-mediating transfection systems. Biochem. Biophys. Res. Commun. *235*, 726–729. https://doi.org/10.1006/bbrc.1997.6880.

Perlmutter, J.D., and Hagan, M.F. (2015). Mechanisms of virus assembly. Annu. Rev. Phys. Chem. *66*, 217–239. https://doi.org/10.1146/annurev-physchem-040214-121637.

Provencher, S.W., and Gloeckner, J. (1981). Estimation of globular protein secondary structure from circular dichroism. Biochemistry *20*, 33–37. https://doi.org/10.1021/bi00504a006.

Ramamoorth, M., and Narvekar, A. (2015). Non viral vectors in gene therapy- an overview. J. Clin. Diagn. Res. *9*, GE01–GE06. https://doi.org/10.7860/JCDR/2015/10443.5394.

Requião, R.D., Carneiro, R.L., Moreira, M.H., Ribeiro-Alves, M., Rossetto, S., Palhano, F.L., and Domitrovic, T. (2020). Viruses with different genome types adopt a similar strategy to pack nucleic acids based on positively charged protein domains. Sci. Rep. *10*, 5470. https://doi.org/10.1038/s41598-020-62328-w.

Riley, R.S., June, C.H., Langer, R., and Mitchell, M.J. (2019). Delivery technologies for cancer immunotherapy. Nat. Rev. Drug Discov. *18*, 175–196. https://doi.org/10.1038/s41573-018-0006-z.

Rossmann, M.G. (2013). Structure of viruses: a short history. Q. Rev. Biophys. *46*, 133–180. https://doi.org/10.1017/S0033583513000012.

Rucker, A.L., and Creamer, T.P. (2002). Polyproline II helical structure in protein unfolded states: lysine peptides revisited. Protein Sci. *11*, 980–985. https://doi.org/10.1110/ps.4550102.

Scott, E.A., Stano, A., Gillard, M., Maio-Liu, A.C., Swartz, M.A., and Hubbell, J.A. (2012). Dendritic cell activation and T cell priming with adjuvant- and antigen-loaded oxidation-sensitive polymersomes. Biomaterials *33*, 6211–6219. https://doi.org/10.1016/j.biomaterials.2012.04.060.

Shi, B., Zheng, M., Tao, W., Chung, R., Jin, D., Ghaffari, D., and Farokhzad, O.C. (2017). Challenges in DNA delivery and recent advances in multifunctional polymeric DNA delivery systems. Biomacromolecules *18*, 2231–2246. https://doi.org/10.1021/acs.biomac.7b00803.

Shirley, J.L., de Jong, Y.P., Terhorst, C., and Herzog, R.W. (2020). Immune responses to viral gene therapy vectors. Mol. Ther. *28*, 709–722. https://doi.org/10.1016/j.ymthe.2020.01.001.

Smith, T.R.F., Patel, A., Ramos, S., Elwood, D., Zhu, X., Yan, J., Gary, E.N., Walker, S.N., Schultheis, K., Purwar, M., et al. (2020). Immunogenicity of a DNA vaccine candidate for COVID-19. Nat. Commun. *11*, 2601. https://doi.org/10.1038/s41467-020-16505-0.

Song, H., Yu, M., Lu, Y., Gu, Z., Yang, Y., Zhang, M., Fu, J., and Yu, C. (2017). Plasmid DNA delivery: nanotopography matters. J. Am. Chem. Soc. *139*, 18247–18254. https://doi.org/10.1021/jacs.7b08974.

Srivastava, A., Mallela, K.M.G., Deorkar, N., and Brophy, G. (2021). Manufacturing challenges and rational formulation development for AAV viral vectors. J. Pharm. Sci. *110*, 2609–2624. https://doi.org/10.1016/j.xphs.2021.03.024.

Stack, T., Liu, Y., Frey, M., Bobbala, S., Vincent, M., and Scott, E. (2021). Enhancing subcutaneous injection and target tissue accumulation of nanoparticles via co-administration with macropinocytosis inhibitory nanoparticles (MiNP). Nanoscale Horiz. *6*, 393–400. https://doi.org/10.1039/D0NH00679C.

Stack, T., Vincent, M., Vahabikashi, A., Li, G., Perkumas, K.M., Stamer, W.D., Johnson, M., and Scott, E. (2020). Targeted delivery of cell softening micelles to schlemm's canal endothelial cells for treatment of glaucoma. Small *16*, 2004205. https://doi.org/10.1002/smll.202004205.

Stewart, M.P., Sharei, A., Ding, X., Sahay, G., Langer, R., and Jensen, K.F. (2016). In vitro and ex vivo strategies for intracellular delivery. Nature *538*, 183–192. https://doi.org/10.1038/nature19764.

Summerton, J.E. (2005). Endo-Porter: a novel reagent for safe, effective delivery of substances into cells. Ann. N Y. Acad. Sci. *1058*, 62–75. https://doi.org/10.1196/annals.1359.012.

Tiffany, M.L., and Krimm, S. (1968). Circular dichroism of poly-L-proline in an unordered conformation. Biopolymers *6*, 1767–1770. https://doi.org/10.1002/bip.1968.360061212.

Tifany, M.L., and Krimm, S. (1972). Effect of temperature on the circular dichroism spectra of polypeptides in the extended stateEffwct of temperature on the circular dichroism spectra of polypeptides in the extended state. Biopolymers *11*, 2309–2316. https://doi.org/10.1002/bip.1972.360111109.

Uversky, V.N., Gillespie, J.R., and Fink, A.L. (2000). Why are "natively unfolded" proteins unstructured under physiologic conditions? Proteins *41*, 415–427. https://doi.org/10.1002/1097-0134(20001115)41:3<415::AID-PROT130>3.0.CO;2-7.

Uversky, V.N., Oldfield, C.J., and Dunker, A.K. (2005). Showing your ID: intrinsic disorder as an ID for recognition, regulation and cell signaling. J. Mol. Recognit. *18*, 343–384. https://doi.org/10.1002/jmr.747.

van der Loo, J.C.M., and Wright, J.F. (2016). Progress and challenges in viral vector manufacturing. Hum. Mol. Genet. *25*, R42–R52. https://doi.org/10.1093/hmg/ddv451.

Vasdekis, A.E., Scott, E.A., O'Neil, C.P., Psaltis, D., and Hubbell, J.A. (2012). Precision intracellular delivery based on optofluidic polymersome rupture. ACS Nano *6*, 7850–7857. https://doi.org/10.1021/nn302122h.

Vincent, M., and Schnell, S. (2016). A collection of intrinsic disorder characterizations from eukaryotic proteomes. Sci. Data *3*, 160045. https://doi.org/10.1038/sdata.2016.45.

Vincent, M., Whidden, M., and Schnell, S. (2016). Quantitative proteome-based guidelines for intrinsic disorder characterization. Biophys. Chem. *213*, 6–16. https://doi.org/10.1016/j.bpc.2016.03.005.

Vincent, M., Uversky, V.N., and Schnell, S. (2019). On the need to develop guidelines for characterizing and reporting intrinsic disorder in proteins. Proteomics *19*, e1800415. https://doi.org/10.1002/pmic.201800415.

Vincent, M.P., Bobbala, S., Karabin, N.B., Frey, M., Liu, Y., Navidzadeh, J.O., Stack, T., and Scott, E.A. (2021a). Surface chemistry-mediated modulation of adsorbed albumin folding state specifies nanocarrier clearance by distinct macrophage subsets. Nat. Commun. *12*, 648. https://doi.org/10.1038/s41467-020-20886-7.

Vincent, M.P., Karabin, N.B., Allen, S.D., Bobbala, S., Frey, M.A., Yi, S., Yang, Y., and Scott, E.A. (2021b). The combination of morphology and surface chemistry defines the immunological identity of nanocarriers in human blood. Adv. Ther. *4*, 2100062. https://doi.org/10.1002/adtp.202100062.

Vincent, M., and Schnell, S. (2019). Disorder Atlas: Web-based software for the proteome-based interpretation of intrinsic disorder predictions. Comput Biol Chem. *83*, 107090. https://doi.org/10.1016/j.compbiolchem.2019.107090.

Vincent, M.P., Stack, T., Vahabikashi, A., Li, G., Perkumas, K.M., Ren, R., Gong, H., Stamer, W.D., Johnson, M., and Scott, E.A. (2021c). Surface engineering of FLT4-targeted nanocarriers enhances cell-softening glaucoma therapy. ACS Appl. Mater. Interfaces *13*, 32823–32836. https://doi.org/10.1021/acsami.1c09294.

Vincent, M.P., Navidzadeh, J.O., Bobbala, S., and Scott, E.A. (2022). Leveraging self-assembled

nanobiomaterials for improved cancer immunotherapy. Cancer Cell *40*, 255–276. https://doi.org/10.1016/j.ccell.2022.01.006.

Wang, B., Merillat, S.A., Vincent, M., Huber, A.K., Basrur, V., Mangelberger, D., Zeng, L., Elenitoba-Johnson, K., Miller, R.A., Irani, D.N., et al. (2016). Loss of the ubiquitin-conjugating enzyme UBE2W results in susceptibility to early postnatal lethality and defects in skin, immune, and male reproductive systems. J. Biol. Chem. *291*, 3030–3042. https://doi.org/10.1074/jbc.M115.676601.

Wang, S., and Chen, R. (2017). pH-responsive, lysine-based, hyperbranched polymers mimicking endosomolytic cell-penetrating peptides for efficient intracellular delivery. Chem. Mater. *29*, 5806–5815. https://doi.org/10.1021/acs.chemmater.7b00054.

Xu, X., Jian, Y., Li, Y., Zhang, X., Tu, Z., and Gu, Z. (2014). Bio-inspired supramolecular Hybrid dendrimers self-assembled from low-generation peptide dendrons for highly efficient gene delivery and biological tracking. ACS Nano *8*, 9255–9264. https://doi.org/10.1021/nn503118f.

Yang, J.-P., and Huang, L. (1997). Overcoming the inhibitory effect of serum on lipofection by increasing the charge ratio of cationic liposome to DNA. Gene Ther. *4*, 950–960. https://doi.org/10.1038/sj.gt.3300485.

Yi, S., Allen, S.D., Liu, Y.-G., Ouyang, B.Z., Li, X., Augsornworawat, P., Thorp, E.B., and Scott, E.A. (2016). Tailoring nanostructure morphology for enhanced targeting of dendritic cells in atherosclerosis. ACS Nano *10*, 11290–11303. https://doi.org/10.1021/acsnano.6b06451.

Yi, S., Zhang, X., Sangji, M.H., Liu, Y., Allen, S.D., Xiao, B., Bobbala, S., Braverman, C.L., Cai, L., Hecker, P.I., et al. (2019). Surface engineered polymersomes for enhanced modulation of dendritic cells during cardiovascular immunotherapy. Adv. Funct. Mater. *29*, 1904399. https://doi.org/10.1002/adfm.201904399.

Yip, B.H. (2020). Recent advances in CRISPR/Cas9 delivery strategies. Biomolecules *10*, 839. https://doi.org/10.3390/biom10060839.

Zeng, H., Johnson, M.E., Oldenhuis, N.J., Tiambeng, T.N., and Guan, Z. (2015). Structure-based design of dendritic peptide bolaamphiphiles for siRNA delivery. ACS Cent. Sci. *1*, 303–312. https://doi.org/10.1021/acscentsci.5b00233.

Zhang, Y., Satterlee, A., and Huang, L. (2012). In vivo gene delivery by nonviral vectors: overcoming hurdles? Mol. Ther. *20*, 1298–1304. https://doi.org/10.1038/mt.2012.79.

Zhou, D., Cutlar, L., Gao, Y., Wang, W., O'Keeffe-Ahern, J., McMahon, S., Duarte, B., Larcher, F., Rodriguez, B.J., Greiser, U., and Wang, W. (2016). The transition from linear to highly branched poly(β-amino ester)s: branching matters for gene delivery. Sci. Adv. *2*, e1600102. https://doi.org/10.1126/sciadv.1600102.

STAR★METHODS

KEY RESOURCES TABLE

REAGENT or RESOURCE	SOURCE	IDENTIFIER
Chemicals, peptides, and recombinant proteins		
Dendritic peptide (DP) with the sequence of {[(RHL)2-KRHL]2-KRHL}, 2-KC-NH2	Peptide 2.0 Inc.	https://www.peptide2.com/
Poly(ethylene glycol) methyl ether (Average Mn∼2000)	Sigma-Aldrich	202509
Poly(ethylene glycol) methyl ether (Average Mn750)	Sigma-Aldrich	202495
Toluene	Sigma-Aldrich	179418
Dichloromethane	Sigma-Aldrich	34856
Triethylamine	Sigma-Aldrich	471283
Methanesulfonyl chloride	Sigma-Aldrich	471259
Diethyl ether	Sigma-Aldrich	673811
Dimethylformamide	Sigma-Aldrich	227056
Potassium carbonate	Sigma-Aldrich	209619
Thioacetic acid	Sigma-Aldrich	8.08076
Tetrahydrofuran	Sigma-Aldrich	34865
Sodium methoxide	Sigma-Aldrich	403067
Propylene sulfide	TCI	1072-43-1
2,2-dithiodipyridine	Sigma-Aldrich	43791
Water (molecular biology grade)	Sigma-Aldrich	W4502
DMEM medium	Thermo Fisher Scientific	A4192101
RPMI 1640 medium	Thermo Fisher Scientific	A4192301
Penicillin-Streptomycin	Thermo Fisher Scientific	15140122
Fetal bovine serum	Thermo Fisher Scientific	10082147
2-Mercaptoethanol	Sigma-Aldrich	516732
GM-CSF Recombinant Protein	Thermo Fisher Scientific	PMC2016
IL-4 Recombinant Protein	Thermo Fisher Scientific	RP-8666
L-glutamine	Sigma-Aldrich	59202C
GelRed® Nucleic Acid Stain 1000X Water	Millipore	SCT123
Thiazoly Blue Tetrazolium Bromide (MTT)	Sigma-Aldrich	M5655
NucBlue™ Live Ready Probes™ Reagent	Invitrogen™	R37605
Critical commercial assays		
ACK Lysing Buffer	Gibco	A1049201
Lipofectamine™ 2000 Transfection Reagent	Invitrogen™	11668030
Ulysis™ Alexa Fluor™ 488 Nucleic Acid Labeling Kit	Invitrogen™	U21650
Experimental models: Cell lines		
RAW 264.7	ATCC	TIB-71™
NIH 3T3	ATCC	CRL-1658™
Jurkat	ATCC	TIB-152™
DH5α competent cells	Thermo Fisher Scientific	18263012
Recombinant DNA		
pCMV-DsRed (4.6 kb)	Clonetech	632539
pcDNA3.1 (5.4 kb)	Thermo Fisher Scientific	V79020
pL-CRISPR.EFS.tRFP	Addgene	Plasmid #57819

(*Continued on next page*)

Continued

REAGENT or RESOURCE	SOURCE	IDENTIFIER
Software and algorithms		
FlowJo™ v10	BD Biosciences	https://www.flowjo.com/
GraphPad Prism 8	GraphPad	https://www.graphpad.com/

RESOURCE AVAILABILITY

Lead contact

Further information and requests should be directed to the lead contact, Evan Alexander Scott (evan.scott@northwestern.edu).

Materials availability

All data are available in the manuscript text and supplemental information. This study did not generate new unique reagents.

Data and code availability

- All data produced in this study are included in the published article and its supplemental information or are available from the lead contact upon request.
- The paper dose not report original code.

EXPERIMENTAL MODEL AND SUBJECT DETAILS

Generation of mouse primary bone-marrow-derived dendritic cells

To prepare bone-marrow-derived dendritic cells (BMDCs), bone marrow cells were collected from the tibias and femurs of naïve C57Bl/6 mice (Jackson Laboratory) (Napoli et al., 2001). Mouse tibia and femur bones were removed and sterilized by soaking in 70% ethanol for 5 min on ice. The bones were then transferred from ethanol to a sterile culture dish containing filtered primary media (RPMI 1640 medium supplemented with 10% fetal bovine serum (FBS), penicillin (100 IU/mL) and streptomycin (100 mg/mL), B-Me (50 Um), L-Gln (2 mM), GM-CSF (20 ng/mL), and IL-4 (10 ng/mL)). Both ends of the bone were cut off and flush out the bone marrow using a sterile syringe. Transfer cells to a sterile 15mL falcon tube and centrifuge at 1500 rpm for 10 min. The cell pellets were resuspended in 1mL of ACK lysing buffer (Thermo Fisher Scientific) to remove red blood cells. After wash cells with sterile PBS, the cells were then resuspended in primary media and counted. Cells were cultured in 100 mm Petri dishes with a density of 1×10^6 cells/mL and incubated at 37°C with 5% CO_2 for seven days. After 7 days, non-adherent and loosely adherent cells (imDCs) were harvested, washed, and used for *in vitro* experiments.

METHOD DETAILS

Plasmids

All plasmids were propagated in DH5α competent cells (Thermo Fisher Scientific). The plasmid DNA concentration was determined using a NanoDrop 2000 instrument (Thermo Fisher Scientific) by measuring the absorbance at 260 nm.

Synthesis of PEG-b-PPS-s-s-DP (PPDP) polymers

The poly(ethylene glycol) (PEG)-based initiator was prepared by thioacetate modification of methoxy PEG-OH (MW = 750 or 2000).(Cerritelli et al., 2007, 2009b; Scott et al., 2012; Yi et al., 2016). Poly(ethylene glycol) methyl ether ($mPEG_{17}$, MW = 750 or $mPEG_{45}$, MW = 2000) (20 mmol, 1 equiv.) was dissolved in toluene and dried by azeotropic distillation. The dried mPEG was cooled to room temperature under vacuum and dissolved in dichloromethane (50 mL). The reaction vessel was evacuated and subsequently purged with argon (Ar). Triethylamine (5 equiv.) was added and cooled to 0°C. Methanesulfonyl chloride (5 equiv.) was diluted into dichloromethane (100 mL) and added dropwise to the cooled solution. After stirring overnight under Ar, the mixture was filtered to remove salt, and dichloromethane was removed by rotary evaporation. The obtained product was precipitated in cold diethyl ether and dried under vacuum. The mesylate-functionalized mPEG (6.0 g, 1 equiv.) was dissolved in anhydrous dimethylformamide (DMF, 100 mL)

within a Ar-evacuated three-neck flask. Potassium carbonate (5 equiv.) and thioacetic acid (5 equiv.) were added. After stirring overnight, salt was removed by filtration and DMF was removed by rotary evaporation. The obtained product was dissolved in tetrahydrofuran (THF) and passed through an aluminum oxide column. The thioacetate-functionalized mPEG was then precipitated in cold diethyl ether and dried under vacuum. PEG thioacetate initiators (0.5 g, 1 equiv.) were transferred to Schlenk tube under argon and dissolved in dimethylformamide (DMF) (6 mL). Sodium methoxide (0.5 M solution in methanol, 1.2 equiv.) was added using syringe. After stirring for 30 min, the amount of propylene sulfide (PPS) used in the reaction was adjusted to polymerize the desired block lengths. The polymerization was end-capped by adding excess 2,2-dithiodipyridine (5 equiv.) and stirring overnight. The obtained block copolymers (PEG_{17}-*b*-PPS_{80}-pds, PEG_{17}-*b*-PPS_{51}-pds, PEG_{17}-*b*-PPS_{42}-pds, PEG_{45}-*b*-PPS_{74}-pds, PEG_{45}-*b*-PPS_{48}-pds, PEG_{45}-*b*-PPS_{25}-pds) were then purified by double precipitation in cold methanol or diethyl ether. All the polymers were characterized by ^{1}H NMR ($CDCl_3$). The dendritic peptide (DP) was conjugated to different PEG-*b*-PPS polymers via disulfide exchange. PEG-*b*-PPS (50–100 mg) was reacted with DP (1.2 equiv) in triethylamine/dimethylformamide (DMF) (0.1/1 mL). The peptide-polymer conjugates were purified by repeat precipitation in cold diethyl ether to remove 2-pyridienthione. The vacuum-dried peptide-polymer conjugates were dispersed in water (molecular biology grade) and then dialyzed against water using Slide-A-Lyzer Dialysis Cassettes (20K MWCO, Thermo Fisher Scientific) to remove unreacted peptide. Following purification, the PEG-PPS-ss-DP conjugates were lyophilized.

Preparation of PPDP nanostructures

A variety of PPDP polymers were used in these studies, including: PEG_{17}-*b*-PPS_{80}-ss-DP (PPDP2), PEG_{17}-*b*-PPS_{51}-ss-DP (PPDP3), PEG_{17}-*b*-PPS_{42}-ss-DP (PPDP4), PEG_{45}-*b*-PPS_{74}-ss-DP (PPDP5), PEG_{45}-*b*-PPS_{48}-ss-DP (PPDP6), and PEG_{45}-*b*-PPS_{25}-ss-DP (PPDP7). The specified PPDP polymer was dissolved in water (molecular biology grade) to prepare a stock solution at a 10 mg/mL polymer concentration. Plasmid DNA-PPDP nanocomplexes (DNA-PPDP) were formed by diluting both PPDPs vectors and pDNA solutions with water to a volume of 50 μL, and were subsequently mixed at a polymer-to-DNA mass ratio (w/w) ranging from 1 to 120. The resulting DNA-PPDP complexes were formed by gentle pipetting for 30 s, followed by a 30-min incubation step at room temperature.

Characterization of PPDP nanostructure morphology and physicochemical properties

The size distribution and zeta potential of the PPDP nanostructures were measured using a Zetasizer Nano instrument (Malvern Instruments). Cryogenic transmission electron microscopy (Cryo-TEM) was performed to characterize nanostructure morphology. Briefly, 200-mesh lacey carbon grids were glow-discharged for 30 s in a Pelco easiGlow glow-discharger (Ted Pella Inc.) at 15 mA with a chamber pressure of 0.24 mBar. Grids were prepared with 4 μL of sample and were plunge-frozen into liquid ethane using a FEI Vitrobot Mark III cryo plunge freezing device for 5 s with a blot offset of 0.5 mm. After plunge-freezing, grids were loaded into a Gatan 626.5 cryo transfer holder and were imaged at −172°C in a JEOL JEM1230 LaB6 emission TEM (JEOL USA, Inc.) at 100kV. Data was acquired using a Gatan Orius 2k x 2k camera.

Small angle x-ray scattering (SAXS)

SAXS was performed at the DuPont-Northwestern-Dow Collaborative Access Team (DND-CAT) beamline at the Advanced Photon Source (APS) at Argonne National Laboratory (Argonne, IL, USA). A ~7.5 m sample-to-detector distance was used. Silver behenate diffraction patterns were used to calibrate the q-range. Samples were irradiated with 10 keV x-rays using a 3 s exposure time. Data was analyzed in the 0.001–0.5 Å. PRIMUS 2.8.3 and SasView 5.0 software was used for data reduction and model fitting, respectively. Core shell sphere models were fit to the data. Modeling was performed following established procedures(Stack et al., 2020; Vincent et al., 2021a, 2021b).

Characterization of pH-dependent peptide conformational changes

FT-IR spectra were acquired by A Nicolet iS50 FTIR Spectrometer (Thermo Scientific). Spectra were obtained for liquid samples of PPDP2, peptide, and PEG-*b*-PPS. 64 scans were collected per sample in the 2000–600 cm^{-1} range. For the circular dichroism (CD) spectroscopy studies, PEG-*b*-PPS, Peptide and PPDP2 were prepared in water with pH adjusted to 5.5, 6.5, and 7.5 prior to analysis. Samples were prepared in quartz cuvette (0.1 cm path length) and CD spectroscopy was performed using a Jasco J-815 CD Spectrometer. Data was collected via a continuous scan in the 190–300 nm wavelength range using

a 100 nm/min scanning speed, a 2 s digital integration time, 2 nm band width, and a 0.5 nm data pitch. The high tension (HT) voltage was monitored to ensure data was collected in the linear range (Figure S8).

Electrophoretic mobility shift assay (EMSA)

The stability of PPDP/pDNA nanocomplexes was determined by EMSA. PPDP/pDNA nanocomplexes were prepared at different weight ratios of PPDPs to pDNA, as described elsewhere in this STAR Methods section. The same amount of pDNA (0.5 μg) was used for each sample. The obtained nanocomplexes (10 μL) were mixed with loading buffer and loaded on 1% agarose gel containing GelRed® nucleic acid stain submerged in Tris-acetic acid-EDTA (TAE) buffer (40 mM Tris-base, 20 mM acetic acid, 1 mM sodium EDTA). Electrophoresis was carried out at a constant voltage of 100 V for 30 min (Bio-Rad, Inc.). Gels were imaged using a LAS 4010 Gel Imaging system (GE Healthcare).

Cell viability assay

The relative viability of cells transfected with various PPDPs/pDNA, Lipofectamine 2000/pDNA complexes (Lipo2K), PEI/pDNA complexes (PEI with the molecular weight of 25 kDa), and Dendritic peptide (DP1)/pDNA complexes were determined using the 3-(4,5-dimethylthiazol-2-yl)-2,5-diphenyltetrazolium bromide (MTT) assay. Cells were plated in 96-well plates at a seeding density of 30,000 cells per well in 100 μL of culture medium. The cells were then treated under the specified conditions for an incubation period of 24 h (with 0.2 μg of DNA): naked pDNA, Lipofectamine 2000/DNA, PEI (25 kDa)/DNA (w/w from 5:1 to 10:1), DP1/DNA (w/w from 10:1 to 50:1), PPDP2/DNA (w/w from 30:1 to 120:1), PPDP3/DNA (w/w from 30:1 to 120:1), PPDP4/DNA (w/w from 30:1 to 120:1), PPDP5/DNA (w/w from 30:1 to 120:1), PPDP6/DNA (w/w from 30:1 to 120:1), PPDP7/DNA (w/w from 30:1 to 120:1). After 24 h, cells were incubated with the MTT reagent (5 mg/mL in PBS, 10 μL per well) for 4 h. DMSO (200 μL) was used to dissolve the resulting formazan crystals formed in each well. The absorbance of 560 nm light was measured using a SpectraMax M3 multi-mode microplate reader (Molecular Devices, LLC). Cell viability was calculated as the percent viability compared to untreated controls.

Cell transfection *in vitro*

The pCMV-DsRed (4.6 kb) was used as a small plasmid and pL.CRISPR.EFS.tRFP (11.7 kb) was used as a large plasmid in these studies. RAW 264.7, BMDCs, and Jurkat cells were plated at 10^5 cells/well and NIH 3T3 fibroblasts were plated at 5×10^4 cells/well in 24-well plates. For each transfection sample, PPDP-plasmid DNA nanocomplexes (PPDP/DNA) were prepared as follows. Dilute stock solution of PPDP (3 μL of 10 mg/mL PPDP in 50 μL PRMI or DMEM medium without serum) and plasmid DNA stock solution (0.25 μL of 2 mg/mL pDNA in PRMI or DMEM medium without serum). The PPDP/DNA nanocomplexes were prepared by adding 50 μL diluted PPDP suspension into 50 μL diluted pDNA solution. The resulting PPDP/DNA nanocomplexes were formed by gentle pipetting for 30 s, and then incubated at room temperature for 30 min. Lipofectamine 2000-pDNA complexes were prepared according to the manufacture's instructions. Briefly, dilute plasmid DNA stock solution (0.25 μL of 2 mg/mL pDNA in 50 μL PRMI or DMEM medium without serum) and mix gently. Dilute Lipofectamine 2000 1 μL in 50 μL PRMI or DMEM medium without serum, and mix gently. After 5 min incubation, combine the diluted pDNA with the diluted Lipofectamine 2000, mix gently, and incubate for 20 min at room temperature. The 100 μL of naked plasmids, Lipo2K/DNA, PPDP2/DNA, PPDP3/DNA, PPDP4/DNA, PPDP5/DNA, PPDP6/DNA, PPDP7/DNA (w/w 60:1 for PPDP/DNA) suspension was mixed with 400 μL complete medium with serum and added to each well (500 ng plasmid in 500 μL medium per well). After a 48 h transfection period, the transfection efficiency (percentages of DsRed+ and RFP + cells) and the mean fluorescence intensity (MFI) were quantified by flow cytometry using a BD LSRFortessa 6-Laser flow cytometer (BD Biosciences). FlowJo software was used to analyze the acquired flow cytometry data. For confocal microscopy analysis, RAW 264.7 and NIH 3T3 cells were plated at 10^4 cells/well in 8-well Chamber slides (Thermo Fisher Scientific) and were cultured for 24 h before use. Cells were then transfected with a naked plasmid, Lipo2K/DNA, and PPDP2/DNA (w/w 60:1 for PPDP2/DNA), respectively, with 500 ng plasmid per well. After 48 h, cells were counterstained with NucBlue™ Live ReadyProbes™ Reagent (nuclei stain, one drop) for 15 min in the dark. Images were acquired on a Leica TCS SP8 confocal microscope with a 40X oil immersion objective.

Cellular internalization analysis

Small plasmid DNA (pcDNA3.1, 5.4 kb) was fluorescently labeled with Alexa Fluor 488™ Ulysis™ Nucleic Acid Labelling Kit (Thermo Fisher Scientific) using manufacturer procedures. RAW 264.7 cells were

prepared at 20,000 cells per well in 8-well Chamber slides (Thermo Fisher Scientific) and were cultured for 24 h before use. Alexa Fluor 488-labeled pDNA (488-DNA) was mixed with PPDP2 (w/w 60:1 for PPDP2: plasmid), or Lipo2K (v/w 6 μL/μg for Lipo2K: plasmid) as described above. The obtained 488-pDNA PPDP2 complexes (488-pDNA-PPDP2), 488-pDNA, and 488-pDNA-Lipo2K were incubated with cells for 1, 4, or 18 h incubation periods, as specified. The concentration of 488-pDNA was 1 μg/mL for each well. After incubation, cells were washed twice with PBS and were subsequently incubated with LysoTracker™ Red DND-99 (1:5000 dilution, 300 μL DMEM) for 30 min. Afterwards, the cells were washed twice with PBS, and were incubated with NucBlue™ Live ReadyProbes™ Reagent (nuclei stain, 1 drop) in 300 μL PBS per well for 15 min in the dark. Images were acquired on a Leica TCS SP8 confocal microscope with a 63X oil immersion objective.

QUANTIFICATION AND STATISTICAL ANALYSIS

GraphPad Prism software (version 8) was used for data analysis. Data are presented as mean ± SD. Significance was determined using an appropriate statistical test, as described in the corresponding figure legends.